

Rapid X-ray Variability in Mkn 421 during a Multiwavelength Campaign

Alex G. Markowitz,^{1,2} Krzysztof Nalewajko,¹ Gopal Bhatta,³ Gulab C. Dewangan,⁴ Sunil Chandra,^{5,6} Daniela Dorner,⁷ Bernd Schleicher,⁷ Urszula Pajdosz-Śmierciak,⁸ Łukasz Stawarz,⁸ Staszek Zola,^{8,9} Michał Ostrowski,⁸ Daniele Carosati,^{10,11} Saikruba Krishnan,¹ Rumen Bachev,¹² Erika Benítez,¹³ Kosmas Gazeas,¹⁴ David Hiriart,¹⁵ Shao-Ming Hu,¹⁶ Valeri Larionov,^{17,18} Alessandro Marchini,¹⁹ Katsura Matsumoto,²⁰ A.A. Nikiforova,^{17,18} Tapio Pursimo,²¹ Claudia M. Raiteri,²² Daniel E. Reichart,²³ Diego Rodriguez,²⁴ Evgeni Semkov,¹² Anton Strigachev,¹² Yuki Sugiura,²⁰ Massimo Villata,²² James R. Webb,²⁵ Axel Arbet-Engels,²⁶ Dominik Baack,²⁷ Matteo Balbo,²⁸ Adrian Biland,²⁶ Thomas Bretz,^{26,29} Jens Buss,²⁷ Laura Eisenberger,⁷ Dominik Elsaesser,²⁷ Dorothee Hildebrand,²⁶ Roman Iotov,⁷ Adelina Kalenski,⁷ Karl Mannheim,⁷ Alison Mitchell,²⁶ Dominik Neise,²⁶ Maximilian Noethe,²⁷ Aleksander Paravac,⁷ Wolfgang Rhode,²⁷ Vitalii Sliusar,²⁸ and Roland Walter²⁸

¹Nicolaus Copernicus Astronomical Center, Polish Academy of Sciences, ul. Bartycka 18, 00-716 Warszawa, Poland

²University of California, San Diego, Center for Astrophysics and Space Sciences, MC 0424, La Jolla, CA, 92093-0424, USA

³Institute of Nuclear Physics, Polish Academy of Sciences, 31-342 Kraków, Poland

⁴Inter-University Centre for Astronomy and Astrophysics, Post Bag 4, Ganeshkhind, Pune 411007 India

⁵Tata Institute of Fundamental Research, Mumbai, India

⁶Centre for Space Research, North-West University, Private Bag X6001, Potchefstroom, 2520, South Africa

⁷University of Würzburg, Institute for Theoretical Physics and Astrophysics, Emil-Fischer-Straße 31, Campus Hubland Nord, 97074, Würzburg, Germany

⁸Astronomical Observatory of the Jagiellonian University, ul. Orła 171, 30-244 Kraków, Poland

⁹Mt. Suhora Observatory, Pedagogical University, ul. Podchorążych 2, 30-084 Kraków, Poland

¹⁰EPT Observatories, Tijarafe, E-38780 La Palma, Spain

¹¹INAF, TNG Fundación Galileo Galilei, E-38712 La Palma, Spain

¹²Institute of Astronomy and National Astronomical Observatory, Bulgarian Academy of Sciences, 72 Tsarigradsko Shosse Blvd., 1784 Sofia, Bulgaria

¹³Universidad Nacional Autónoma de México, Instituto de Astronomía, AP 70-264, CDMX 04510, Mexico

¹⁴Section of Astrophysics, Astronomy and Mechanics, Department of Physics, National and Kapodistrian University of Athens, GR-15784, Zografos, Athens, Greece

¹⁵Instituto de Astronomía, Universidad Nacional Autónoma de México, AP106, 22860 Ensenada, BC, Mexico

¹⁶Shandong Key Laboratory of Optical Astronomy and Solar-Terrestrial Environment, Institute of Space Sciences, School of Space Science and Physics, Shandong University, Weihai, Shandong, 264209, China

¹⁷Astronomical Institute, St. Petersburg State University, 198504, St. Petersburg, Russia

¹⁸Pulkovo Observatory, 196140, St. Petersburg, Russia

¹⁹University of Siena, Department of Physical Sciences, Earth and Environment, Astronomical Observatory, Via Roma 56, I-53100 Siena, Italy

²⁰Osaka Kyoiku University, Institute of Astronomy, 4-698-1 Asahigaoka, Kashiwara 582-8582, Osaka, Japan

²¹Nordic Optical Telescope, Apartado 474, E-38700 Santa Cruz de La Palma, Spain

²²INAF, Osservatorio Astrofisico di Torino, via Osservatorio 20, I-10025 Pino Torinese, Italy

²³University of North Carolina at Chapel Hill, Dept. of Physics and Astronomy, Chapel Hill, NC, 27599, USA

²⁴Guadarrama Observatory, E-28430 Alpedrete, Madrid, Spain

²⁵Department of Physics, Florida International University, 11200 SW 8th St., Miami, FL, 33199, USA, and SARA Observatory

²⁶ETH Zurich, Institute for Particle Physics and Astrophysics, Otto-Stern-Weg 5, 8093 Zurich, Switzerland

²⁷TU Dortmund, Experimental Physics 5, Otto-Hahn-Str. 4a, 44227 Dortmund, Germany

²⁸University of Geneva, Department of Astronomy, Chemin d'Ecogia 16, 1290 Versoix, Switzerland

²⁹also at RWTH Aachen University

ABSTRACT

The study of short-term variability properties in AGN jets has the potential to shed light on their particle acceleration and emission mechanisms. We report results from a four-day coordinated multi-wavelength campaign on the highly-peaked blazar (HBL) Mkn 421 in January 2019. We obtained X-ray data from AstroSAT, BVRI photometry with the Whole Earth Blazar Telescope (WEBT), and TeV data from FACT to explore short-term multi-wavelength variability in this HBL. The X-ray continuum is rapidly variable on time-scales of tens of ks. Fractional variability amplitude increases with energy across the synchrotron hump, consistent with previous studies; we interpret this observation in the context of a model with multiple cells whose emission spectra contain cutoffs that follow a power-law distribution. We also performed time-averaged and time-resolved (time-scales of 6 ks) spectral fits; a broken power-law model fits all spectra well; time-resolved spectral fitting reveals the usual hardening when brightening behaviour. Intra-X-ray cross correlations yield evidence for the 0.6–0.8 keV band to likely lead the other bands by an average of 4.6 ± 2.6 ks, but only during the first half of the observation. The source displayed minimal night-to-night variability at all wavebands thus precluding significant interband correlations during our campaign. The broadband SED is modeled well with a standard one-zone leptonic model, yielding jet parameters consistent with those obtained from previous SEDs of this source.

Key words: BL Lacertae objects: Mkn 421 – galaxies: active – acceleration of particles – black hole physics

1 INTRODUCTION

Blazars are a subset of Active Galactic Nuclei (AGN) whose luminosity is dominated by emission from a relativistic jet lying close to the line of sight (Urry & Padovani 1995). These jets emit non-thermal, Doppler-boosted emission across the electromagnetic spectrum, with a characteristic broad two-hump spectral energy distribution (SED). One hump, typically peaking in IR-optical-UV, is synchrotron emission from relativistic electrons. The other hump typically peaks in γ -rays, with leptonic (Inverse Compton) and hadronic emission processes under consideration (Mannheim 1993; Böttcher et al. 2013). Classically, blazars have been broadly categorized based on optical spectral properties and on SEDs into the more luminous Flat-Spectrum Radio Quasars, with strong emission lines, strong Compton dominance, and synchrotron emission typically peaking $\sim 10^{13-14}$ Hz, and BL Lac type objects (BL Lacs), which are lower power and have synchrotron emission peaking typically $\sim 10^{14-16}$ Hz. BL Lacs can be further divided into high- and low-peaked BL Lacs (HBL/LBL) based on synchrotron peak frequency. More recent classification schemes for all blazars – low-/intermediate-/high-peaked blazars – are also based on SED peak frequencies (Abdo et al. 2010). Strong continuum variability on time-scales from minutes to years (e.g., Ulrich, Maraschi, & Urry 1997; Pian 2002; Bhatta et al. 2016; Bhatta & Dhital 2020) is observed across all blazar sub-classes. Open issues to explore include determining the exact location of the emission zones for each band and the dominant particle acceleration processes, e.g., propagating shocks, magnetic reconnection, and the role of magnetic turbulence (Mastichiadis & Kirk 1997; Böttcher & Dermer 2010; Yan et al. 2013; Sironi, Petropoulou, & Giannios 2015). Jets likely derive their power from rotational energy of spinning supermassive black holes (e.g., Blandford & Znajek 1977; Sikora et al. 2005), though launching and collimation mechanisms remain unclear. Insight into jet structure as well as emission mechanisms comes from dedicated multi-wavelength (MWL) continuum flux and polarization moni-

toring campaigns that enable us to search for interband correlations and model the time-dependent behaviour of the SED, particularly towards relatively short time-scales.

In HBLs, X-ray and TeV are thought to both probe the highest-energy population of electrons, as supported by commonly-observed correlations between X-ray and TeV bands, as well as variability amplitude increasing with energy within each SED hump. Mkn 421 is one of the most famous HBL/HSP blazars: it was the first extragalactic-confirmed TeV source (Punch et al. 1992), and has been targeted by MWL campaigns of varying spectra/temporal coverage and involving a wide range of space- and ground-based telescopes. Its flux density can span up to two orders of magnitude in many bands, though it is known to usually be bright at optical, X-ray, and TeV wavebands, and frequently displays rapid ($<1-2$ day) variability in the X-ray and TeV wavebands (e.g., Błażejowski et al. 2005; Giebels, Dubus, & Khélifi 2007; Abdo et al. 2011; Aleksić et al. 2015b; Baloković et al. 2016).

Variability as short as minutes–sub-hours in X-ray and γ -rays has been observed in Mkn 421 and other HBLs, suggesting these bands probe the most energetic electrons, which have shortest cooling times (e.g., Aharonian et al. 2007; Ackermann et al. 2016). In Mkn 421, X-ray/TeV emission is generally correlated on time-scales of week/months/years, usually at zero time lag, across multiple flux levels (e.g., Amenomori et al. 2003; Rebillot et al. 2006; Albert et al. 2007; Aleksić et al. 2015b; Baloković et al. 2016; Ahnen et al. 2016; Arbet-Engels et al. 2021), though Fossati et al. (2008) observed a 2.1 ± 0.7 ks X-ray-to-TeV lag during a strong flare in 2001. Such strong correlations are also observed in other HBLs (e.g., Mkn 501, Krawczynski et al. 2000, 2002). Combined with SED modeling, these correlations generally support a one-zone synchrotron self-Compton (SSC) scenario (e.g., Acciari et al. 2011; Aleksić et al. 2012; Abeysekara et al. 2017), though hadronic models may also be relevant (Böttcher et al. 2013).

Meanwhile, optical to TeV/X-ray correlations are only sometimes seen in HBLs, and are not a common property; the optical band probes lower electron energies ($\nu_{\text{syn}} \propto \gamma^2$), and the optical emitting region likely has a higher volume filling factor than X-

* Email: almarkowitz@camk.edu.pl

ray/TeV. Furthermore, some campaign results on Mkn 421 support multiple compact regions, e.g., two-zone SSC models: Correlated X-ray/TeV flares, poorly correlated with optical emission, observed during a 13-day MWL campaign in 2010 were fit by two distinct blobs (Aleksić et al. 2015b; see also Baloković et al. 2016). Similarly, observations of optical polarization degree (PD) not correlating simply with flux or wide rotations of position angle (PA) also support multiple emission regions (Carnerero et al. 2017) with different volumes and/or differing electron energy distribution (EED) widths. An additional complication is the occasional observation of TeV orphan flares in Mkn 421 (and other HBLs, e.g., Acciari et al. 2011), or an X-ray orphan flare (e.g., Rebillot et al. 2006; Lichti et al. 2008; Acciari et al. 2020); such flares mandate either fine-tuning of SSC models (Krawczynski et al. 2004), alternate models such as a spine/sheath configuration (Ghisellini, Tavecchio, & Chiaberge 2005), or gamma rays produced by hadrons (e.g., proton-synchrotron emission, Mücke & Protheroe 2001).

We thus organized a coordinated multi-wavelength campaign in X-rays, TeV, and optical/NIR occurring 2019 January 10–14, MJD 58493 – 58497. This was a campaign planned in advance, and not organized in response to any target of opportunity alert. Our strategy here is to concentrate on short time-scale variability characteristics in Mkn 421, using a continuous 4-day campaign. Our science goals are to build up a more complete physical picture of the jet, including the properties of emitting regions.

The rest of the paper is organized as follows: §2 describes the observations and data reduction, including extraction of light curves and spectra. In §3, we explore continuum variability within separate bands, including variability amplitudes. Cross-correlations are presented in §4. In §5, we present the results of time-averaged and time-resolved X-ray spectral fits. The FACT TeV spectra are presented in §6, and we present our broadband SED in §7. We present a discussion of the results in §8, and a summary of our main conclusions in §9.

2 OBSERVATIONS AND DATA REDUCTION

2.1 AstroSat

AstroSat (Singh et al. 2014) is the first dedicated Indian astronomy mission aimed at studying celestial sources in X-ray, UV and limited optical spectral bands simultaneously. It was launched from Satish Dhawan Space Centre, Sriharikota on 28 September 2015 into a 650 km near-equatorial orbit with 6-degree orbital inclination; this orbital inclination helps to minimize (though not eliminate) passage through the South Atlantic Anomaly on most orbits. *AstroSat* is operated by the Indian Space Research Organisation (ISRO).

AstroSat contains five payloads spanning the optical/UV and soft–hard X-ray ranges; in this paper, we use data from the Soft X-ray Telescope (SXT) and Large Area Xenon Proportional Counters (LAXPC). Unfortunately, we could not use the Ultraviolet Imaging Telescopes to observe Mkn 421 in the UV range; an extremely bright star in the UVIT field of view would have violated the instrument’s safety threshold.

AstroSat continuously observed Mkn 421 from 07:47 UT on 2019 January 10 to 18:59 UT on 2019 January 14, for a duration of 68 orbits (orbit numbers 17764–17831), with time lost only to Earth occultation occurring every 97 minutes.

2.1.1 SXT reduction

The SXT¹ (Singh et al. 2017) is a focusing telescope with conical foil mirrors and an X-ray CCD detector; it covers the 0.3–7 keV range. Level 1 data were reprocessed to produce cleaned level 2 events; to do this, we used SXT software version 1.4b², including the GTI corrector and event merger Julia script SXTEVTMERG-ERTOOL³. We used Xselect v. 2.4g in HEASOFT v. 6.26 to extract a time-averaged spectrum; we extracted counts from a 16′ radius circle centered on the source. We also extracted time-resolved spectra, one for each orbit. We extracted background-subtracted light curves over the 0.6–7 keV band and the 0.6–0.8, 0.8–1.1, 1.1–1.4, 1.4–1.9, 1.9–3.0, and 3.0–7.0 keV sub-bands, which we then binned to the satellite orbit (5830 s); we did not detect significant variability on shorter time-scales. A blank-sky SXT spectrum (Sky-Bkg_comb_EL3p5_Cl_Rd16p0_v01.pha), provided by the SXT team, was used to estimate background count rates within each sub-band. In all spectral fits, we use the “gain” command to modify the response and alleviate calibration issues associated with modeling the instrumental Si K and Au M edges near ~ 1.8 and ~ 2.2 keV, respectively; the gain slope was fixed to 1. All SXT spectra were fit over the 0.6–7.0 keV range. We used the latest response and effective area files provided by the SXT team for sources observed on-axis: sxt_pc_mat_g0to12.rmf and sxt_pc_excl00_v04_20190608.arf.

2.1.2 LAXPC reduction

The LAXPC consists of three large-area (~ 6000 cm²) X-ray proportional counter units, each with a time resolution of 10 μs and covering the 3–80 keV range (Yadav et al. 2016; Agrawal et al. 2017). For this observation, we used data from LAXPC unit 2 only. Unit 3 was switched off in March 2018 due to abnormal gain changes. Unit 1 underwent high voltage adjustments in Spring 2018, and so standard response files cannot be applied; we may include unit 1 data in a future analysis when updated response files are made available by the LAXPC Team.

We used the 2018 May 19 Format A version of the LAXPC software⁴, and we reprocessed level 1 events using LAXPC_MAKE_EVENT to generate cleaned level 2 event files. We refer the reader to Antia et al. (2017) for further details on response matrix generation and model-based estimation of background spectra. We extracted a time-average spectrum, as well as time-resolved spectra, one for each orbit; again, no significant variability on shorter time-scales was confirmed. Spectra were initially extracted in 1024 channels but rebinned to an energy resolution of 5 per cent (three times higher than the LAXPC energy resolution). We also extracted background-subtracted and orbitally-binned light curves over the 3–7, 7–12, and 12–20 keV bands. The 3–7 keV LAXPC light curve agreed well with the 3–7 keV SXT light curve in terms of their variability trends. However, while those trends were also present in the 7–12 and 12–20 keV bands, these latter two bands showed additional variability trends not observed < 7 keV. These additional trends matched very well with variability trends detected at > 40 keV, where the source is not significantly detected, and are thus likely artefacts of background modeling and subtraction. For example, the 12–20 keV net and background count rates are 3.2 and 12.3 ct s^{−1}, respectively;

¹ https://www.tifr.res.in/~astrosat_sxt/index.html

² www.tifr.res.in/~astrosat_sxt/sxt_pipeline.php

³ http://www.tifr.res.in/~astrosat_sxt/dataanalysis.html

⁴ <http://astrosat-ssc.iucaa.in/?q=laxpcData>

~ 2 per cent background fluctuations (the expected level of systematic uncertainty in background modeling, e.g., Antia et al. 2017) would cause spurious fluctuations of up to ~ 8 per cent in the net light curve, consistent with the observed net light curve. We thus avoided using the > 7 keV light curve data for this object, and restricted spectral fitting to < 7 keV. In all spectral fits, we use the “gain” command to modify the response and alleviate calibration issues, with the gain slope fixed to 1.

2.2 FACT

The First G-APD Cherenkov Telescope⁵ (FACT), an imaging air-Cherenkov telescope located on the Canary Island La Palma in Spain, is monitoring blazars at TeV energies (Anderhub et al. 2013). Using silicon-based photosensors (Biland et al. 2014), the duty cycle of the instrument is maximized while at the same time the gaps in the light curves are minimized. Mkn 421, Mkn 501, 1ES 1959+650 and 1ES 2344+51.4, the brightest blazars at TeV energies, are observed on a nightly basis within the visibility windows for about 120 to 200 nights per year. A total of up to 2600 hours of physics data are recorded per year (Dorner et al. 2019).

Usually the blazars are observed between 40 minutes and 6 hours per night depending on their visibility, where the schedule is maximized for best threshold. However, for the January 2019 campaign on Mkn 421, the observation windows were maximized for the 5 nights of the campaign (2019 January 10 – 14, morning UTC time) to increase the simultaneous coverage with *AstroSat* and WEBT.

The data were analysed using the Modular Analysis and Reconstruction Software (MARS) (Bretz & Dorner 2010) with the low level analysis as described in Dorner et al. (2015). For the background suppression, the “light curve cuts” and the “spectrum cuts” as described in Beck et al. (2019) were applied correspondingly to calculate the light curves and spectra. To correct the light curves for observational effects, the dependence of the gamma ray rate from zenith distance and trigger threshold (changing with ambient light conditions) was determined using the gamma ray rate measured from the Crab Nebula, a standard candle at TeV energies. Correction factors were applied to the light curves as described in Arbet-Engels et al. (2021).

To select good quality data, a selection cut based on the cosmic-ray rate (Beck et al. 2019; Hildebrand et al. 2017) using the artificial trigger rate R_{750} was applied. Choosing a threshold of 750 DAC-counts, the dependence of R_{750} on the zenith distance was studied and a corrected rate $R_{750,\text{cor}}$ was determined as described in Mahlke et al. (2017) and Bretz (2019). To take into account seasonal changes of the cosmic-ray rate due to changes in the Earth’s atmosphere, a reference value $R_{750,\text{ref}}$ was determined per moon period. Good quality data were selected using $0.93 < R_{750,\text{cor}}/R_{750,\text{ref}} < 1.3$. After data quality selection, the following data sampling is obtained: 4.9, 5.5, 5.0, 4.4, and 4.5 hours for 10, 11, 12, 13, and 14 Jan., respectively.

2.3 WEBT

The Whole Earth Blazar Telescope⁶ (WEBT) is a global network of observatories which routinely coordinate to conduct uninterrupted campaigns on blazars to explore their short time-scale variability

characteristics (e.g., Villata et al. 2002; Raiteri et al. 2017). Sixteen observatories in the WEBT consortium contributed to this campaign (listed in Table 1). The target was observed in four wide band Johnson-Cousins photometric system filters: *B*, *V*, *R*, and *I* (where available), with effective central wavelengths of 4353, 5477, 6349, and 8797 Å, respectively. Exposure times for individual images ranged from 30 to 1600 s, depending on the telescope parameters.

The standard calibration method has been applied to all of the acquired images (bias, dark and flat-field images correction). The Skynet telescopes’ raw data were calibrated with the software provided by The Skynet Robotic Telescope Network (Zola et al. 2021), while for the rest of the images we used Image Reduction & Analysis Facility (IRAF)⁷. The C-MUNIPACK package⁸ was used to perform differential aperture photometry by a single person (U.P.-S.) to ensure uniformity in the results. The comparison star was at RA = 11^h 04^m 51^s.14, Dec=+38° 17′ 10″.8 from Villata et al. (1998); the check stars are located at RA = 11^h 04^m 18^s.18, Dec=+38° 16′ 31″.1 from Villata et al. (1998) or RA = 11^h 04^m 08^s.48, Dec=+38° 22′ 26″.5 from McGimsey, Miller, & Willamon (1976) (all are epoch J2000). To achieve consistent results, we chose the radius of photometry aperture based on the pixel scale of each instrument’s CCD camera. Because of bad quality, some data have been excluded from further analysis.

For the purpose of analysis of fractional variability amplitudes, we selected the observations from the EPT Observatory, La Palma; this observatory’s *V*, *R*, and *I* band light curves had the best sampling – continuously for durations ranging from 15.5 to 23.4 ks (4.3 to 6.5 hours) each night for four consecutive nights – and yielded the best variability-to-noise ratio. For the purpose of constructing the broadband SED, however, we used all data to compute time-averaged magnitudes in *B*, *V*, *R*, and *I* bands, and converted to flux densities using zeropoints from Bessell, Castelli, & Plez (1998).

We corrected the derived flux densities for optical extinction due to the Galaxy, $N_{\text{H,tot}} = 2.03 \times 10^{20} \text{ cm}^{-2}$ (Willingale et al. 2013), and using the dust/gas extinction ratio of Nowak et al. (2012), $N_{\text{H}} = A_{\text{V}} \times 2.69 \times 10^{21} \text{ cm}^{-2} \text{ mag}^{-1}$, which yields $A_{\text{V}} = 0.05 \text{ mag}$. Following the Galactic extinction curve of Cardelli, Clayton, & Mathis (1989), $A_{\text{B}} \sim 1.2A_{\text{V}} = 0.06 \text{ mag}$, $A_{\text{R}} \sim 0.8A_{\text{V}} = 0.04 \text{ mag}$, and $A_{\text{I}} \sim 0.6A_{\text{V}} = 0.03 \text{ mag}$. The *B*, *V*, *R*, and *I* band flux densities were multiplied by 1.06, 1.05, 1.04, and 1.03, respectively.

We estimated and subtracted the contamination from the elliptical host galaxy: Carnerero et al. (2017) estimated the R-band contamination in the host galaxy to be 7.86 mJy for a 5 arcsec aperture. Following a de Vaucouleurs profile (Eqn. 1 in Carnerero et al. 2017), we estimate that a 4 arcsec aperture would see a contamination level of 5.37 mJy, which is 33 per cent of the total (jet + host galaxy) flux observed during our campaign. We applied the colour indices of Mannucci et al. (2001) for elliptical galaxies ($B - V = 0.99 \pm 0.05$, $V - R = 0.59 \pm 0.05$, and $V - I = 1.22 \pm 0.07$) to estimate the level of contamination at *B* band (1.66 mJy; 17 per cent of total observed flux), *V* band (3.70 mJy; 26 per cent of total), and *I* band (7.57 mJy; 38 per cent of total). Fractional variability amplitudes (defined and calculated in §3.1) for *V*, *R*, and *I* bands were subsequently increased by factors of 1.35, 1.50, and 1.61, respectively.

The final time-averaged flux densities for the jet at *B*, *V*, *R*,

⁵ <https://fact-project.org/>

⁶ <https://www.oato.inaf.it/blazars/webt/>

⁷ <http://ast.noao.edu/data/software>

⁸ <http://c-munipack.sourceforge.net/>

and I bands were 7.99, 10.45, 10.70, and 12.41 mJy, respectively; fluxes in units of $\text{erg cm}^{-2} \text{s}^{-1}$ are listed in Table 2.

2.4 Fermi

We extracted a contemporaneous GeV spectrum using data from the *Fermi* Large Area Telescope (LAT; Atwood et al. 2009). Data were analysed with the ScienceTools software package (v11r5p3) using the instrument response function (IRF) P8R2_SOURCE_V6. LAT events were selected from the region of interest (ROI) of radius 10° centered at Mkn 421. We have established that for events detected over the time period of MJD = 58493 – 7 with reconstructed arrival direction $< 2^\circ$ from Mkn 421, the maximum reconstructed energy was 7.9 GeV, hence we restricted the analysis to the energy range of (0.1 – 8) GeV. We applied selection cuts for good time intervals (GTI), avoiding the South Atlantic Anomaly (SAA), using zenith angles $< 100^\circ$. Our source model includes sources from the 3FGL catalog (Acero et al. 2015) located within 20° from Mkn 421, but only those that had been detected over a longer time period of MJD = 58450 – 58550 with test statistic $TS > 1$; it also includes the Galactic background template gll_iem_v06, and the isotropic background spectrum iso_P8R2_SOURCE_V6_v06. In the maximum likelihood analysis, the spectrum of Mkn 421 was fitted with the PowerLaw2 model.

We did not extract a light curve (e.g., daily-binned), as the variability-to-noise ratio was too low for meaningful constraints on variability amplitudes or interband correlations.

3 OVERVIEW OF MULTIBAND VARIABILITY

SXT sub-band light curves, normalized by their means, are presented in Fig. 1. There is a quasi-sinusoid-like trend dominating the variability in our campaign. However, given the small number of cycles observed and the known propensity of red noise variability processes in all categories of AGN, such a trend does not constitute evidence of a quasi-periodic signal and is consistent with a pure red noise process (e.g., Vaughan et al. 2016), as discussed further in Appendix A.

It is additionally curious that the first couple periods of this quasi-sinusoid-like trend are in the neighborhood of 90 ks (~ 1 day). We thus explored all possible satellite and detector housekeeping parameters to exclude any possible instrumental effect. We found no correlation with satellite attitude, satellite passage through the South Atlantic Anomaly, charged particle background rate (as measured by the on-board Charged Particle Monitor), satellite pointing offsets or roll angle, quality grade of SXT operating conditions, nor any detector operational parameters (e.g., CCD and camera temperatures). We conclude that this trend is intrinsic to Mkn 421.

Following e.g., Baloković et al. (2016), we characterized the typical variability time-scale by fitting each rise/fall in the 1.1–1.4 keV light curve (which has the highest count rate of the SXT sub-bands) with an exponential rise/decay, e.g., $F(t) = e^{-t/\tau_{\text{var}}}$. We find the mean τ_{var} in this band to be 130 ks.

The > 0.7 TeV FACT corrected flux light curve is presented, overplotted with re-normalized SXT light curves, in Fig. 2. Neither the TeV nor the X-ray band shows strong day-to-day variation during the duration of our campaign, though there are TeV variability trends observed on \sim hour time-scales on some nights. Potential X-ray/TeV interband correlations are explored further in §4.2.

The I-, R-, and V-band differential magnitude photometric data points obtained at the EPT telescope are plotted in Fig. 3. The

maximum/minimum flux ratios are quite small, only ~ 0.3 per cent in I-band and ~ 0.6 per cent in R-band, and not atypical for Mkn 421.

3.1 Variability amplitudes

We calculated fractional variability amplitude F_{var} (Vaughan et al. 2003) for each *AstroSat* SXT band and for the WEBT/EPT I-, R-, and V-bands (in flux units, not magnitudes); the results are listed in Table 2. At $\sim 9 - 15$ per cent, our values are bit lower than typical values for F_{var} in X-rays on timescales of \sim days ($\sim 40 - 80$ per cent, e.g., Giebels, Dubus, & Khélifi 2007; Baloković et al. 2016; Acciari et al. 2020, albeit at different flux states). Within the X-ray band, F_{var} increases monotonically with photon energy; F_{var} also increases with energy from the NIR/optical (of the X-rays, as illustrated in Fig. 4. We find best-fitting relations (in log-log space) of $F_{\text{var}} \propto E^{0.20 \pm 0.01}$ (NIR/optical + X-ray) or $F_{\text{var}} \propto E^{0.26 \pm 0.02}$ (X-ray only).

Our results are qualitatively consistent with previous measurements of F_{var} increasing with energy in HBL blazars across the X-ray band (e.g., references in Ulrich, Maraschi, & Urry 1997; Kataoka et al. 2000), and qualitatively consistent with measurements of F_{var} increasing within each SED hump in Mkn 421 and Mkn 501 (Giebels, Dubus, & Khélifi 2007; Baloković et al. 2016; Schleicher et al. 2019; Acciari et al. 2020; Arbet-Engels et al. 2021), although Acciari et al. (2020) noted such behaviour occurring in most, but not all, of their observations. Our results are qualitatively consistent with Giebels, Dubus, & Khélifi (2007), who measured $F_{\text{var}} \propto E^{1/4}$ from optical to UV to X-rays and with Fossati, Celotti, & Chiaberge (2000), who found $F_{\text{var}} \propto E^{-1/4}$ across the X-ray band. We must note caveats against such direct comparisons of F_{var} , however, given the slightly different window functions: Here, our light curves have durations of ~ 4 days, while the durations of Giebels, Dubus, & Khélifi (2007) and Fossati, Celotti, & Chiaberge (2000) are 1–7 days and 2.3 days, respectively. In addition, as noted by Fossati, Celotti, & Chiaberge (2000, their §4.3.1), there may very well be different flux probability distributions between different campaigns; F_{var} also implicitly assumes a Gaussian distribution, which does not apply to typical blazar light curves (e.g., Emmanoulopoulos, McHardy, & Papadakis 2013).

In the TeV band, using 40 minute-binned light curves, and not omitting the negative-flux points, we measure $F_{\text{var}} = 38.9 \pm 12.1$ per cent. This value is somewhat low compared to what others have measured over timescales of \sim days in the TeV range (e.g., very roughly 40 per cent to above 100 per cent Baloković et al. 2016; Acciari et al. 2020).

3.2 Fitting of individual X-ray flares

We divided each sub-band light curve into four separate flares, each one encompassing a rise and a decay. We ignored the first 67 ks of data (decay only), and define four flare start/stop times within each sub-band light curve by the minima closest to 67, 150, 240, 295, and 355 ks since the start of the observation.

For each separate flare, we removed the baseline “slope” by subtracting a linear trend connecting the end points; we did not fit with an additional linear component with free parameters as that would have added two additional free parameters. We then fit a model following Acciari et al. (2020, their Eq. 5):

$$F(t) = \frac{2A}{2^{-\left\{\frac{t-t_{\text{peak}}}{t_{\text{doub}}}\right\}} + 2^{+\left\{\frac{t-t_{\text{peak}}}{t_{\text{half}}}\right\}}} \quad (1)$$

Contributing Optical Observatories					
	Number of Exposures				Dates
Observatory/Telescope	<i>B</i>	<i>V</i>	<i>R</i>	<i>I</i>	(JD – 2458000.0)
EPT Observatory, 40 cm, Tijarafe, La Palma, Spain		76	89	88	494, 495, 496, 497
Univ. of Athens Obs. (UOAO), 40 cm, Greece			314		492, 499, 501, 502
Astron. Obs., Univ. of Siena, Italy	36	47	34	73	495, 498
Osaka Kyoiku Univ. Obs., 51 cm, Japan		35	38	38	497, 498
NOT-ALFOSC, La Palma		56			496
SARA/Kitt Peak, 90 cm			40		494
PROMPT-5, Cerro Tololo Inter-American Univ., Chile	11	13	9	14	493, 494, 495, 496, 498
PROMPT-8, Cerro Tololo Inter-American Univ., Chile	3	12		15	494, 495, 497
Weihai Obs. of Shadong Univ., 100 cm, China	4	8	9		498
Guadarrama Observatory, 25 cm, Alpedrete, Madrid, Spain		7	6	4	496, 497
PROMPT-MO-1, Meckering Obs., Australia	2	5	2	8	496, 497, 498
RRRT, Fan Mountain Observatory, Virginia, USA	2		6	8	494
St. Petersburg Univ., 40 cm, Russia	3	3	3	4	496
Astron. Obs. Belgrade, 60 cm, Serbia		4	4	4	488, 491
Inst. of Astron. and NAO, Rozhen Obs., 50/70 cm, Bulgaria	2	2	2	2	496
San Pedro Martir Observatory, 84 cm, Mexico			2		495, 496

Table 1. The WEBT observatories/telescopes contributing to the January 2019 campaign.

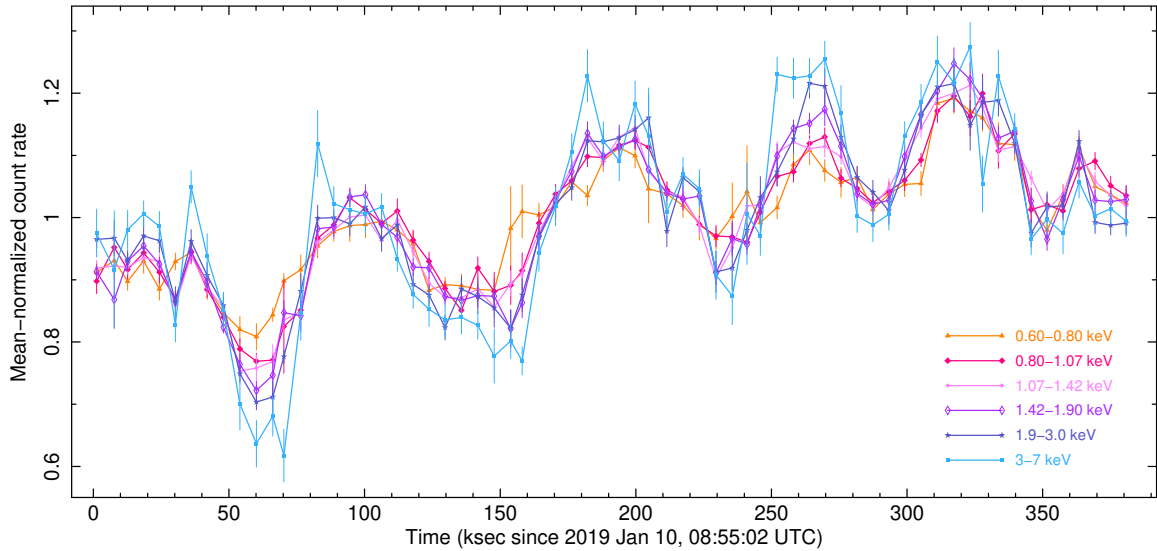


Figure 1. Mean-normalized, orbitally-binned *AstroSAT* SXT light curves.

The four free parameters t_{peak} , t_{doub} , t_{half} , and A denote, respectively, the time of peak flux, the flux-doubling time-scale, the flux-halving time-scale, and the flare amplitude. Results are listed in Table 3, and the flare fits are plotted in Fig. 5. Uncertainties on one parameter with the other three all free are always exceptionally large due to strong parameter degeneracies and relatively small numbers of data points (best-fitting values of the χ^2 statistic were frequently much less than 1, suggesting over-parametrization of the data, especially in flares 3 and 4); the uncertainties on parameters listed in Table 3 were therefore determined by holding the other three frozen at their best-fitting values. Nonetheless, some trends are apparent: flares 1 and 2 are more symmetric towards relatively softer energies (t_{half} and t_{doub} are similar); towards harder energies, t_{half} increases and t_{doub} decreases. Flares 3 and 4 each proceed in relatively achromatic fashion.

To quantify these trends further, we re-fit each sub-band flare, assuming a common peak time (the average of the best-fitting values

of t_{peak} across all sub-bands for a given flare). In the cases of flares 1 and 2, the values of summed χ^2/dof (listed in Table 3) rose significantly: F -tests indicate that allowing t_{peak} to be a free parameter is statistically significant at the 92.8 and 98.2 per cent confidence levels for flares 1 and 2, respectively. However, for flares 3 and 4, the improvement in fit is not significant (only 85 and 72 per cent confidence, respectively).

4 CROSS-CORRELATIONS

4.1 Intra-X-ray Cross-Correlation Functions

Previous X-ray lag measurements in Mkn 421 covering both soft and hard X-rays (e.g., using *ASCA* or *XMM-Newton* and very hard X-rays (tens of keV; *INTEGRAL*) have yielded a range of results: some flares yield no non-zero lag detection, and others sometimes yield positive or negative lags up to a few ks (e.g., Takahashi et al. 1996; Fossati,

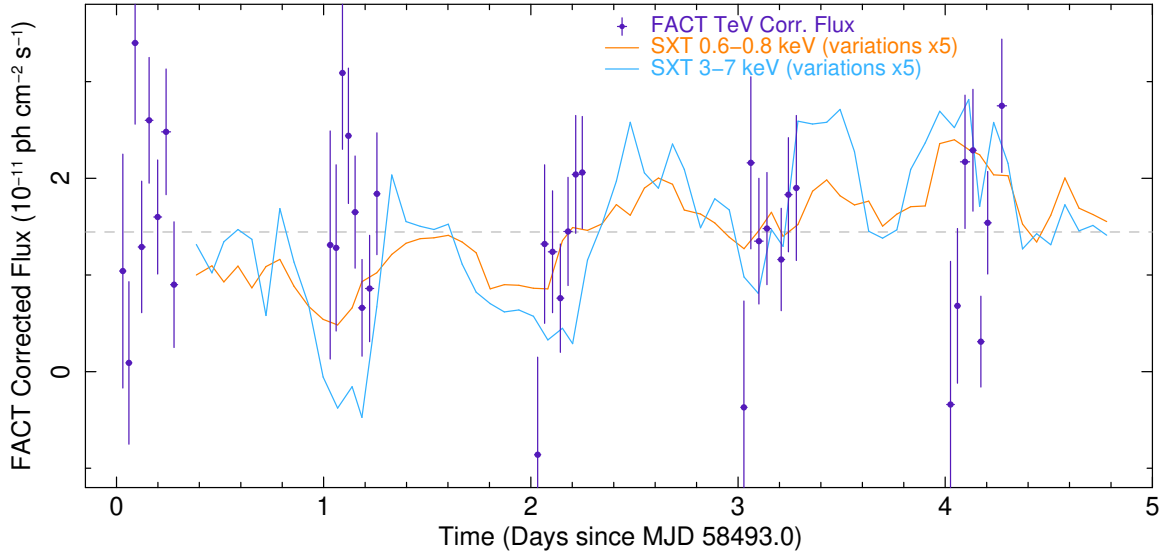


Figure 2. Mean-normalized FACT >0.7 TeV corrected flux light curve, 40-minute bins (purple data points). Overplotted are the *AstroSat* SXT 0.6–0.8 keV (orange line) and 3–7 keV (cyan line) light curves, re-normalized to the mean of the TeV light curve (1.44×10^{-11} ph cm $^{-2}$ s $^{-1}$); variability relative to the mean in the SXT light curves has been amplified by 5 for visualization purposes only.

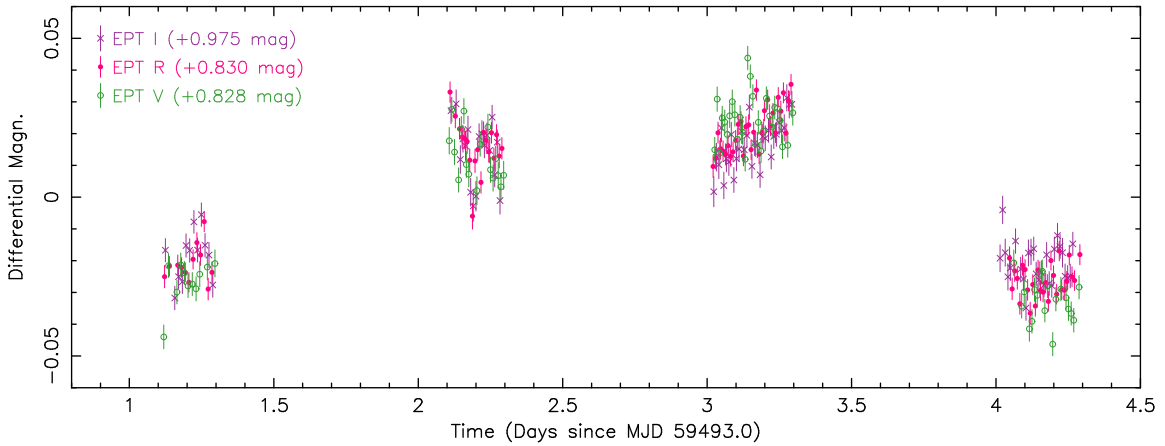


Figure 3. I-, V-, and R-band photometry from the EPT telescope, renormalized to a common differential magnitude.

Variability Amplitudes and Mean Count Rates or Fluxes			
Bandpass	Instrument	Mean	F_{var} (per cent)
<i>I</i>	WEBT	4.67×10^{-11} erg cm $^{-2}$ s $^{-1}$	2.85 ± 0.04 (EPT only)
<i>R</i>	WEBT	5.03×10^{-11} erg cm $^{-2}$ s $^{-1}$	3.15 ± 0.03 (EPT only)
<i>V</i>	WEBT	5.75×10^{-11} erg cm $^{-2}$ s $^{-1}$	3.05 ± 0.04 (EPT only)
<i>B</i>	WEBT	5.43×10^{-11} erg cm $^{-2}$ s $^{-1}$	
0.6–0.8 keV	SXT	1.47 ct s $^{-1}$	8.58 ± 0.32
0.8–1.1 keV	SXT	2.36 ct s $^{-1}$	10.33 ± 0.25
1.1–1.4 keV	SXT	2.71 ct s $^{-1}$	10.96 ± 0.20
1.4–1.9 keV	SXT	2.22 ct s $^{-1}$	11.87 ± 0.24
1.9–3.0 keV	SXT	1.31 ct s $^{-1}$	12.26 ± 0.29
3–7 keV	SXT	0.67 ct s $^{-1}$	15.16 ± 0.45
0.7–11 TeV	FACT (40-min. bins)	1.44×10^{-11} ph cm $^{-2}$ s $^{-1}$	38.9 ± 12.1

Table 2. Variability amplitudes measured over the full duration of each light curve. The third column refers to flux in the case of WEBT (all observatories with good data), mean count rate in the case of *AstroSat* SXT, and mean TeV corrected flux in the case of FACT. Optical fluxes and measurements of F_{var} have been corrected for Galactic foreground absorption and host galaxy contamination. F_{var} was calculated in flux units for the WEBT (EPT-only) light curves.

Flare Fit Parameters								
Band (keV)	Flare start–end (ks)	N_{pts}	t_{doub} (ks)	t_{half} (ks)	t_{peak} (ks)	A (ct s^{-1})	χ^2/dof (t_{peak} free)	χ^2/dof (t_{peak} fixed)
Flare 1								
0.6–0.8	60.1–123.8	12	11.3 ± 1.4	$9.5^{+2.2}_{-1.8}$	97.2 ± 2.3	0.22 ± 0.02	3.07/8	3.66/9
0.8–1.1	60.1–135.7	14	5.6 ± 0.8	13.9 ± 1.1	90.0 ± 1.2	0.50 ± 0.03	13.39/10	14.80/11
1.1–1.4	60.1–135.7	14	7.1 ± 0.9	$11.4^{+0.9}_{-0.8}$	$91.2^{+1.2}_{-1.0}$	0.55 ± 0.03	15.47/10	17.24/11
1.4–1.9	60.1–141.8	15	8.2 ± 0.8	10.1 ± 0.7	92.7 ± 1.0	0.57 ± 0.03	12.65/11	14.78/12
1.9–3.0	60.1–141.8	15	5.0 ± 0.7	$13.1^{+1.1}_{-1.0}$	85.0 ± 1.2	0.31 ± 0.02	12.46/11	14.04/12
3–7	70.3–158.1	16	$1.4^{+0.9}_{-0.7}$	$23.5^{+1.5}_{-1.4}$	$77.7^{+1.0}_{-0.9}$	0.20 ± 0.01	5.82/12	10.80/13
							62.87/62	75.33/68
Flare 2								
0.6–0.8	123.8–229.6	19	$13.2^{+1.8}_{-1.6}$	$8.5^{+1.8}_{-1.6}$	195.6 ± 2.4	0.24 ± 0.02	10.25/15	12.63/16
0.8–1.1	135.7–241.0	19	15.1 ± 1.2	$9.1^{+1.0}_{-0.9}$	196.7 ± 1.4	0.51 ± 0.02	14.48/15	21.08/16
1.1–1.4	135.7–229.6	17	9.1 ± 0.8	13.9 ± 0.9	186.5 ± 1.2	0.67 ± 0.03	32.51/13	35.14/14
1.4–1.9	141.8–229.6	16	4.8 ± 0.9	24.8 ± 1.7	175.7 ± 1.3	0.42 ± 0.02	25.63/12	32.19/13
1.9–3.0	141.8–229.6	16	$5.9^{+1.2}_{-1.0}$	$20.7^{+2.2}_{-2.0}$	180.8 ± 1.7	0.28 ± 0.02	17.53/12	19.39/13
3–7	158.1–235.6	14	$4.6^{+1.0}_{-0.9}$	$24.0^{+2.4}_{-2.1}$	173.7 ± 1.6	0.20 ± 0.01	8.13/10	11.21/11
							108.52/77	131.65/83
Flare 3								
0.6–0.8	229.6–287.4	11	$3.1^{+2.0}_{-1.4}$	$8.8^{+2.4}_{-2.1}$	$259.1^{+2.2}_{-2.3}$	0.15 ± 0.03	1.31/7	1.68/8
0.8–1.1	241.0–287.4	9	$9.2^{+1.7}_{-1.4}$	$3.5^{+1.0}_{-0.9}$	269.7 ± 1.5	0.29 ± 0.03	1.24/5	1.94/6
1.1–1.4	229.6–287.4	11	8.1 ± 1.1	7.7 ± 1.0	$259.6^{+1.6}_{-1.5}$	0.46 ± 0.04	5.81/7	7.06/8
1.4–1.9	229.6–287.4	11	$8.3^{+0.9}_{-0.8}$	4.7 ± 0.7	$266.5^{+1.3}_{-1.2}$	0.43 ± 0.04	4.37/7	5.08/8
1.9–3.0	229.6–293.3	12	8.2 ± 0.9	$4.7^{+0.8}_{-0.7}$	268.7 ± 1.2	0.32 ± 0.03	0.87/8	1.65/9
3–7	235.6–287.4	10	$7.9^{+1.2}_{-1.1}$	$5.7^{+1.0}_{-0.9}$	263.7 ± 1.4	0.23 ± 0.02	3.69/6	4.31/7
							17.30/40	21.71/46
Flare 4								
0.6–0.8	287.4–351.6	12	$4.6^{+1.0}_{-0.9}$	$11.6^{+1.9}_{-1.7}$	314.4 ± 1.6	0.28 ± 0.03	3.69/8	4.22/9
0.8–1.1	287.4–345.7	11	5.2 ± 0.8	$11.2^{+1.0}_{-1.8}$	315.5 ± 1.5	0.41 ± 0.04	5.69/7	6.69/8
1.1–1.4	287.4–351.6	12	6.7 ± 0.8	9.7 ± 1.0	315.8 ± 1.4	0.55 ± 0.04	5.18/8	6.21/9
1.4–1.9	287.4–351.6	12	5.8 ± 0.8	11.6 ± 1.1	314.8 ± 1.2	0.54 ± 0.04	9.13/8	10.52/9
1.9–3.0	293.3–345.7	10	$4.0^{+1.1}_{-1.0}$	$17.7^{+2.7}_{-2.3}$	308.2 ± 1.5	0.25 ± 0.02	5.30/6	6.35/7
3–7	287.4–345.7	11	$4.4^{+1.1}_{-0.9}$	$16.3^{+2.4}_{-2.2}$	307.1 ± 1.7	0.16 ± 0.02	5.92/7	7.03/8
							34.91/44	41.02/50

Table 3. Best-fitting parameters to individual flares following Eqn. 1. Parameter uncertainties correspond to $\Delta\chi^2 = +2.71$ above the best fit. Fits were performed with all four parameters free, yielding the values of χ^2/dof in Col. [8]. We then refit, using t_{peak} fixed at the value averaged across all sub-bands for a given flare, yielding the values of χ^2/dof in Col. [9]; this analysis supports the notion that flares peak at earlier times towards relatively harder X-rays in flares 1 and 2 only.

Celotti, & Chiaberge 2000; Takahashi et al. 2000; Tanihata et al. 2001; Ravasio et al. 2004; Lichti et al. 2008). Measurements of a hard-to-soft lag, could for example, yield information on the cooling time-scale, and therefore a limit on the magnetic field strength, e.g., Chiappetti et al. (1999).

We searched for potential lags/leads between the various sub-band light curves. We remind the reader that, as pointed out by e.g., Tanihata et al. (2001), lags do not necessarily indicate one band "driving" the other as in e.g., Broad Line Region reverberation mapping; in blazars, one is quantifying the energy dependence of decay or rise time-scales of individual flares. We used both the Discrete Correlation Function (DCF; Edelson & Krolik 1988) and the Interpolated Correlated Function (ICF; White & Peterson 1994; based on Gaskell & Sparke 1986). For the DCF, we used a bin time of 5.83 ks (satellite orbital time scale); for the ICF, we used a bin time of 2.915 ks (half an orbit), and we applied the bootstrap error method of Peterson et al. (1998) (both random subset selection

and flux randomization). We explored lags for the entire duration, as well as just for each half of the observation. The results are summarized in Table 4. In all cases, a positive lag indicates that the relatively harder band leads the softer band. We find evidence for the 0.6–0.8 keV band to lead the other bands by an average of 4.6 ± 2.6 ks (from ICF centroids), but only during the first half of the observation. For other waveband combinations, no lags are detected.

From Fig. 1, the softest band visually leads the other bands mostly at local minima, i.e., flares 1 and 2 seem to start a bit earlier in the 0.6–0.8 keV band, consistent with this finding. However, measured lag values are the net sum of all lags/leads within the light curve pair. From the fits to individual flares above, relatively harder bands peak earlier than softer bands during flares 1 and 2. Both positive and negative lag-generating processes are concurrently at work.

When performing cross correlations on pairs of light curves

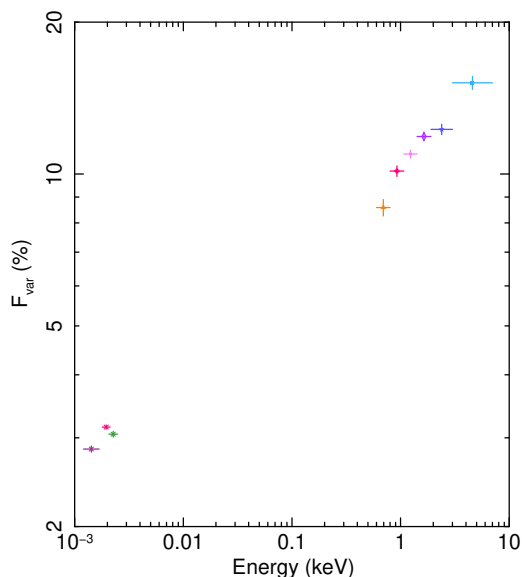


Figure 4. Fractional variability amplitude F_{var} increases monotonically as a function of photon energy across the *AstroSat* SXT bands, and increases with photon energy from the NIR/optical bands to the X-rays.

that suffer from recurring gaps, one must apply caution and confirm that any lags/leads observed have not arisen spuriously as an artefact of the sampling – particularly if the observed lags/leads are on the same order as the periodic gaps (e.g., Takahashi et al. 2000; Edelson et al. 2001; Sembay et al. 2002). Observations using satellites in low-Earth orbit, such as *AstroSat*, can have periodic gaps due to Earth occultations. *AstroSat*’s orbital period is 5.83 ks, a value not far from the 4.6 ± 2.6 ks lag observed from the 0.6–0.8 keV band to the higher-energy bands (we adopt the average of the lags from the 0.6–0.8 keV band to each of the other bands) during the first half of the observation. The fact that only the softest light curve shows a lead while all bands are impacted equally by data gaps might support its divergence from the other bands as being real, but we nonetheless conducted such simulations to assess the impact on the measured lag value.

Here, we perform Monte Carlo simulations, starting with the null hypothesis that the two light curves are intrinsically correlated with zero lag. With the algorithm of Timmer & Koenig (1995), we simulated 500 pairs of light curves, using the same random number seed for each. The input PSD slope was an unbroken power law of slope -2.2 for both light curves, consistent with Chatterjee et al. (2018); the energy dependence of PSD shape within the X-ray band has, to our knowledge, not been explored thoroughly yet so we explore a wider range of slopes below. PSD amplitudes were chosen such that the integral of the PSDs from $1/(194 \text{ ks}) = 5.2 \times 10^{-6} \text{ Hz}$ to the Nyquist frequency of $1/(2 \times 5.3 \text{ ks}) = 8.6 \times 10^{-5} \text{ Hz}$ matched the measured values of F_{var} for the first half of the 0.6–0.8 keV (hereafter “S”) and 1.4–1.9 keV (hereafter “H”) light curves, 7.4 and 10.8 per cent, respectively. We simulated light curves with a time resolution of 100 s (to match the SXT extraction) and a duration of 940 ks, (to allow for red noise leakage), trimmed them to 188 ks, and orbitally binned them in the exact same manner as for the observed light curves. We re-scaled each simulated light curve to match the mean and standard deviation of the S and H light curves. We added Poisson noise by deviating each binned data point by a Gaussian whose standard deviation is equal to the average count rate error within each bin in the observed light curves (0.034 and 0.040 ct s^{-1}

for S and H, respectively). We measured each ICF centroid, and examined the distribution of ICF centroids: only 13/500 trials yields soft-to-hard lags greater than the observed lag lower limit of 2.0 ks (rejection of null hypothesis at 97.4 per cent confidence).

Finally, we explored the potential impact of differing PSD power-law slopes, considering the best-fitting power-law slope values as discussed in Appendix A. We re-simulated the light curve pairs (200 trials), considering power-law slopes of -2.0 for both light curves, -2.4 for both light curves, -2.0 for soft and -2.4 for hard, and -2.4 for soft and -2.0 for hard, each time keeping the PSD normalized to match the observed values of F_{var} , and again including Poisson noise. Again adopting a common observed soft-to-hard lag limit of $+2.0$ ks, we find that for these four cases, we can reject the null hypothesis at 98.5, 95.0, 98.5, and 95.0 per cent confidence, respectively.

Note, however, that all these simulations do not account for the fact that we observed a lag in the first half of the data only; the second half of the data, in which we observed no lag, effectively provides a doubling in the number of trials. To account for this aspect of a “look elsewhere effect” (Algeri et al. 2016), we double the likelihood of the null hypothesis being correct: 94.8, 90.0, 97.0 per cent, (PSD slopes of -2.2 , -2.0 , -2.4 for both bands, respectively), 97.0 and 90.0 per cent (-2.0 for S and -2.4 for H; -2.4 for S and -2.0 for H, respectively).

We conclude that the observed soft-to-hard lag is likely intrinsic to the source and is not an artefact of data sampling or Poisson noise.

4.2 X-ray/TeV Correlated Behaviour

We first searched for lags between the 40-minute binned TeV band and the softest and hardest X-ray bands (0.6–0.8 and 3–7 keV); given the data gaps in the TeV light curve, we used the z-transformed Discrete Correlation Function (zDCF; Alexander 1997, 2013). We do not find any robust evidence for a correlation between the TeV band and either X-ray band, with maximum correlation coefficients remaining below 0.3 on time scales between ± 2 days in both cases. Both zDCFs are plotted in Fig. 6. We additionally explored zero-lag correlations by plotting TeV fluxes as a function of X-ray flux (either soft or hard band), using data points as close as possible to each other in time. Neither across all four nights nor within any one night (where very small-number statistics dominate) do we see any evidence for a correlation.

In conclusion, we cannot claim any TeV–X-ray correlation, in part due to the fact that our campaign simply did not sample strong inter-night variations in either band, and also due to the modest flux level of the source yielding relatively large flux uncertainties within each time bin. Consequently, constraints on whether TeV flux varies proportionally to X-ray flux e.g., in a linear or quadratic fashion are not attainable from these data.

5 X-RAY SPECTRAL MODELING

We first modeled the time-averaged 0.6–7 keV SXT and 3–7 keV LAXPC spectrum. We used Interactive Spectral Interpretation System (ISIS) v.1.6.2-44 for all spectral fitting. We grouped the SXT data to a minimum signal/noise of 5 within ISIS. For all fits, we applied an instrumental cross-normalization constant, frozen to 1 for SXT and allowed to be free for LAXPC. To achieve reasonable fits, we added 2 per cent systematics to both the time-averaged and time-resolved LAXPC spectra.

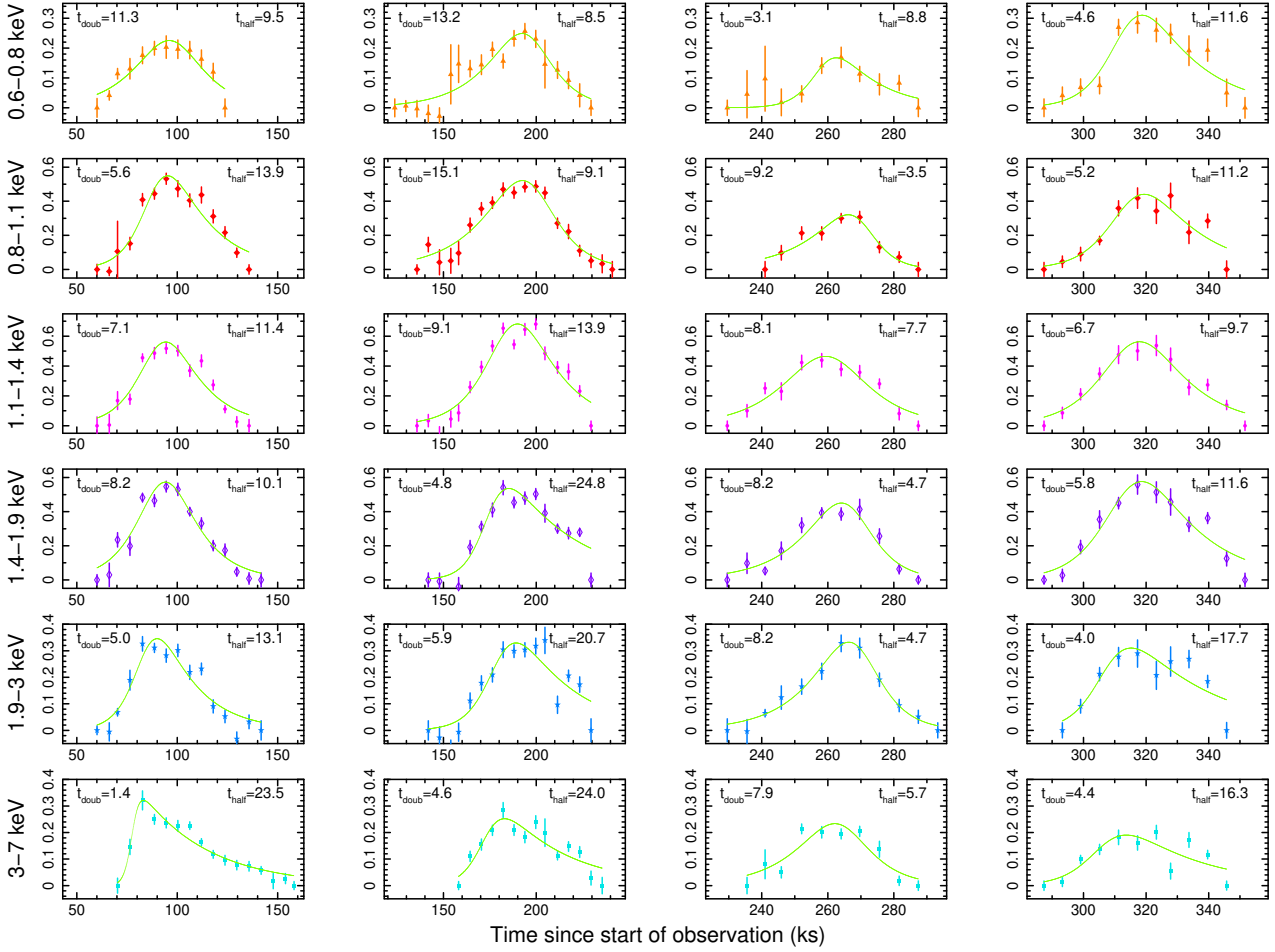


Figure 5. The four individual X-ray flares, fit separately within each sub-band following §3.2. The green line denotes the best-fitting flare model, and best-fitting values of flux doubling (t_{doub}) and halving (t_{half}) time-scales are listed. Flares 1 and 2 (the two left-most columns) have similar rise and decay times only towards the softest energies probed; towards harder energies, t_{half} increases and t_{doub} decreases.

All spectral fits included Galactic absorption accounting for monatomic and molecular hydrogen, $N_{\text{H,tot}} = 2.03 \times 10^{20} \text{ cm}^{-2}$ (Willingale et al. 2013),⁹ and used a redshift value of $z = 0.030021$ (De Vaucouleurs et al. 1991).

5.1 Time-averaged X-ray spectral modeling

All of our model fits to the time-average spectrum yielded large residuals and high values of χ^2_{red} , likely due to strong spectral variability during the observation. Our time-averaged fits thus serve only as an approximate guide for forming an initial model to be applied to the time-resolved spectra in the next subsection.

We first tested a single power law, which yielded $\chi^2/\text{dof} = 1651.68/583 = 2.833$. Our best-fitting model was a broken power law ($\chi^2/\text{dof} = 1590.08/581 = 2.737$), with photon index steepening from $\Gamma_1 = 2.200 \pm 0.005$ below a break energy of $5.0^{+0.3}_{-0.2} \text{ keV}$ to $\Gamma_2 = 2.726^{+0.218}_{-0.134}$ above it, and indicating some slow spectral curvature across the bandpass.

We use the Akaike Information Criterion (AIC; Akaike 1973) with finite sample correction (Sugiura 1978) to ascertain the significance in improvement: For each model, we calculate $AIC =$

$2m - 2C_L + \chi^2 + (2m(m+1))/(n-m-1)$, where m is the number of free parameters (5 for unbroken, 7 for broken), n is the number of data bins (580 for SXT + 8 for LAXPC), and C_L is the likelihood of the true model. We compare the models by computing the difference in values of AIC , so the C_L terms cancel; $\Delta AIC = -57.5$, indicating that the broken power-law model is a better fit. We caution, though, that while preference for this model supports the presence of some spectral curvature, the magnitude of this (phenomenological) spectral break is very strong compared to the best-fitting physically-motivated SED models, discussed in §7. That is, we caution against interpreting the inferred change in slope (~ 0.5) too literally.

Finally, we applied a phenomenological log-parabola fit to model this curvature: $A(E) = K(E(1+z)/E_{\text{pivot}})^{(-a-b\log(E(1+z)/E_{\text{pivot}}))}$; it does not contain a sharp break like the broken power law. We froze E_{pivot} at 0.7 keV. However, our best-fitting model yielded b consistent with zero, a value of a identical to that of Γ in the single power-law fit, and an identical value of χ^2_{red} as well, so we do not discuss log-parabola fits further. The χ residuals for the unbroken and broken power-law models are presented in Fig. 7, and the best-fitting model parameters are listed in Table 5.

⁹ <https://www.swift.ac.uk/analysis/nhtot/index.php>

Intra-X-ray Cross Correlations					
Full Duration					
first	second	DCF r_{corr}	DCF τ (ks)	ICF centroid r_{corr}	ICF centroid τ (ks)
LAX 3–7	SXT 3–7	0.9219±0.0875	0	0.9296	−0.774±1.338
SXT 3–7	SXT 1.9–3	0.9403±0.1128	0	0.9403	+0.340±1.406
SXT 3–7	SXT 1.4–1.9	0.9220±0.0947	0	0.9214	−0.085±1.562
SXT 3–7	SXT 1.1–1.4	0.9044±0.0985	0	0.9040	−0.468±1.592
SXT 3–7	SXT 0.8–1.1	0.8794±0.1059	0	0.8951	+0.650±2.088
SXT 3–7	SXT 0.6–0.8	0.8014±0.1068	0	0.8282	−1.621±2.622
SXT 3–7	SXT 0.6–0.8	0.8014±0.1068	0	0.8282	−1.621±2.622
SXT 1.9–3	SXT 0.6–0.8	0.8874±0.1022	0	0.9090	−1.620±2.169
SXT 1.4–1.9	SXT 0.6–0.8	0.9198±0.0847	0	0.9320	−1.065±1.700
SXT 1.1–1.4	SXT 0.6–0.8	0.9454±0.0801	0	0.9511	−1.030±2.154
SXT 0.8–1.1	SXT 0.6–0.8	0.9417±0.0906	0	0.9598	−2.337±2.100
First Half (0–194 ks)					
first	second	DCF r_{corr}	DCF τ (ks)	ICF centroid r_{corr}	ICF centroid τ (ks)
LAX 3–7	SXT 3–7	0.8892 ± 0.1398	0	0.8990	−0.873±1.675
SXT 3–7	SXT 1.9–3	0.9362 ± 0.0116	0	0.9464	−0.834±1.711
SXT 3–7	SXT 1.4–1.9	0.8740 ± 0.1248	0	0.8963	−1.193±2.003
SXT 3–7	SXT 1.1–1.4	0.8544 ± 0.0898	0	0.8809	−1.835±1.891
SXT 3–7	SXT 0.8–1.1	0.7266 ± 0.1658	−5.8	0.8503	−1.009±2.899
SXT 3–7	SXT 0.6–0.8	0.7631 ± 0.1468	−5.8	0.7648	−5.524±3.206
SXT 3–7	SXT 0.6–0.8	0.7631 ± 0.1468	−5.8	0.7648	−5.524±3.206
SXT 1.9–3	SXT 0.6–0.8	0.8547 ± 0.1626	−5.8	0.8551	−5.044±2.689
SXT 1.4–1.9	SXT 0.6–0.8	0.8776 ± 0.1249	−5.8	0.8816	−4.366±2.314
SXT 1.1–1.4	SXT 0.6–0.8	0.9099 ± 0.1541	−5.8	0.9344	−4.004±2.333
SXT 0.8–1.1	SXT 0.6–0.8	0.9145 ± 0.1667	−5.8	0.9329	−3.926±2.426
Second Half (194–389 ks)					
first	second	DCF r_{corr}	DCF τ (ks)	ICF centroid r_{corr}	ICF centroid τ (ks)
LAX 3–7	SXT 3–7	0.8657 ± 0.1515	0	0.8925	+0.116±1.713
SXT 3–7	SXT 1.9–3	0.8658 ± 0.1170	0	0.8690	+0.856±2.163
SXT 3–7	SXT 1.4–1.9	0.8626 ± 0.1019	0	0.8806	+0.283±1.971
SXT 3–7	SXT 1.1–1.4	0.8179 ± 0.1016	0	0.8219	−0.268±1.950
SXT 3–7	SXT 0.8–1.1	0.7424 ± 0.1376	0	0.8172	+1.357±1.840
SXT 3–7	SXT 0.6–0.8	0.6754 ± 0.1456	0	0.7229	+1.867±2.498
SXT 3–7	SXT 0.6–0.8	0.6754 ± 0.1456	0	0.7229	+1.867±2.498
SXT 1.9–3	SXT 0.6–0.8	0.7855 ± 0.1018	0	0.7890	+0.992±2.350
SXT 1.4–1.9	SXT 0.6–0.8	0.8722 ± 0.1172	0	0.8740	+1.018±2.661
SXT 1.1–1.4	SXT 0.6–0.8	0.8886 ± 0.1177	0	0.8904	+1.295±2.357
SXT 0.8–1.1	SXT 0.6–0.8	0.8915 ± 0.1025	0	0.9052	−1.111±2.478

Table 4. DCF and ICF centroid results. A positive lag indicates the first band leading the second band. Lags not consistent with zero are in bold font. Results indicate that the softest band leads the other bands during the first half of the observation.

5.2 Time-resolved X-ray spectral modeling

We fit only those orbits containing both SXT and LAXPC data, and thus excluded the first orbit (which had LAXPC only) and the last three orbits (SXT only). We first fit a single power-law model to each of the 63 spectra; the average value of χ^2_{red} was 1.20. We then applied a broken power-law model to each spectrum, with Γ_1 , Γ_2 , and E_{break} free but initially set to their best-fitting values from the time-average spectrum. This model yielded a superior fit: the average value of χ^2_{red} fell to 1.05. F -tests performed on each pair of models for each of the 63 orbits always yielded values of F greater than 5.3 and null hypothesis probabilities less than 0.7 per cent (the more complex model always provides a superior fit at the ≥ 99.3 per cent confidence level) for each orbit. We then re-fit the broken power-law model with E_{break} frozen to 4.4 keV, the

mean of the values obtained from the time-resolved fits; the value of χ^2/dof summed across all orbits rose only from 14766.71/13997 to 14801.48/14060, and an F -test indicated that it was not statistically significant to leave this parameter thawed across the sample.

Refitting the time-resolved spectra with Γ_2 fixed to $\Gamma_1 + 0.49$ (the mean values of Γ_1 and Γ_2 in the time-resolved fits above were 2.23 and 2.72, respectively) does not yield a significantly worse set of fits: the summed χ^2/dof rose from 14801.48/14060 to 14870.95/14123, yielding an F -test null hypothesis probability of 0.63. We thus display the results from fits with Γ_2 fixed to $\Gamma_1 + 0.49$ in Fig. 8. The best-fitting linear regression to the Γ_1 versus 0.6–6.0 keV model flux relation follows $\Gamma_1 = (-0.0045 \pm 0.0006)F_{0.6-6} + (2.47 \pm 0.03)$. We also re-plotted the time-resolved spectral fit results of photon index versus time, dividing up the data into four separate flares defined by the minima in the 1.42–1.90 keV

Fits to the Time-Averaged SXT + LAXPC Spectrum		
Parameter	Single Power Law	Broken Power Law
χ^2/dof	1651.68/583=2.833	1590.08/581=2.737
Γ	2.204 ± 0.004	—
Γ_1	—	2.20 ± 0.01
Γ_2	—	$2.726^{+0.22}_{-0.13}$
E_{break} (keV)	—	$5.0^{+0.3}_{-0.2}$
Normalization	0.184 ± 0.001	0.184 ± 0.001
SXT Gain Slope	1.0*	1.0*
SXT Gain Intercept	$0.034^{+0.001}_{-0.002}$	$0.033^{+0.001}_{-0.002}$
LAX Constant	0.88 ± 0.02	0.92 ± 0.02
LAX Gain Slope	1.0*	1.0*
LAX Gain Intercept	$-0.55^{+0.05}_{-0.10}$	-0.37 ± 0.09
0.6–6 keV model flux	5.828×10^{-10} (17.28 mCrb)	5.824×10^{-10} (17.26 mCrb)

Table 5. Normalization refers to the 1 keV normalization ($\text{ph cm}^{-2} \text{s}^{-1} \text{keV}^{-1}$). Model flux here refers to observed/absorbed flux in units of $\text{erg cm}^{-2} \text{s}^{-1}$. An asterisk (*) indicates a frozen parameter.

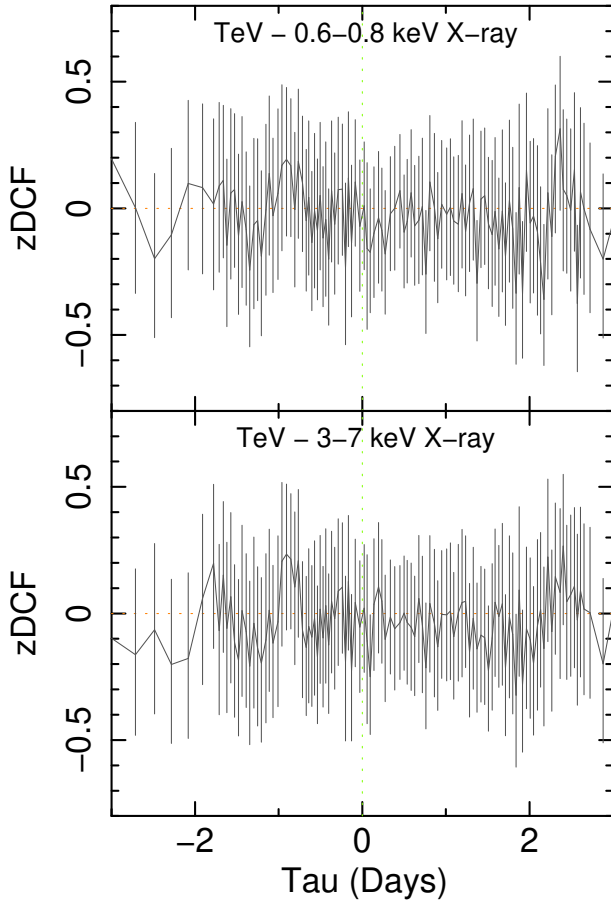


Figure 6. Cross-correlation results for the TeV band (40-minute bins) versus the orbitally-binned soft (0.6–0.8 keV) and hard (3–7 keV) bands. A positive lag indicates TeV leading the X-ray band.

light curve at [60–135], [135–229], [229–286], and [286–353] ks to check for any divergence in their spectral behaviour. However, the spectral and spectral variability behaviour across all flares overlap well.

We tested for any signs of hysteresis in the Γ –flux plane, as has been found for various blazars including Mkn 421 (e.g., [Takahashi et al. 1996](#); [Cui 2004](#); [Abeyssekara et al. 2017](#)), by comparing

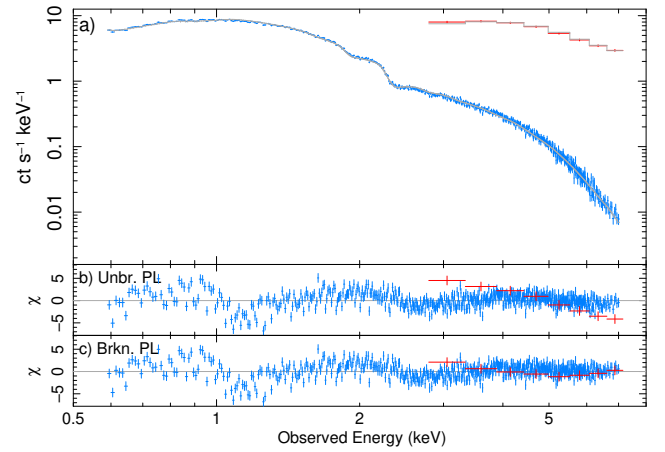


Figure 7. Time-averaged spectral counts data are plotted in panel a). SXT and LAXPC data are shown in blue and red, respectively; the gray lines denote the best-fitting broken power-law model. Panels b) and c) show the residuals to our best-fitting unbroken and broken power-law fits, respectively; most of the improvement in the broken power-law fit compared to the unbroken power-law fit is at higher energies.

values during the rising and decaying flux trends; hysteresis could potentially provide additional insight into cooling and acceleration time-scales. However, no obvious trends were found. Perhaps the range in flux sampled by our campaign was simply too small. Alternatively and speculatively, perhaps there are simultaneous contributions from multiple flares, each in different parts of their hysteresis cycles.

6 TEV SPECTRAL MODELING

We present here the spectrum for the complete campaign as measured by FACT, integrated over 10–14 January. We extracted fluxes in bins above 0.4 TeV in bin widths of 0.2 in the log, though only upper limits for bins > 4 TeV were obtained. The spectrum is plotted in Fig. 9. A least-squares fit to the bins from 0.4 to 4 TeV yields a spectral slope of -2.90 ± 0.16 and a monochromatic 1 TeV normalization of $1.78 \pm 0.16 \times 10^{-11} \text{ ph cm}^{-2} \text{s}^{-1} \text{TeV}^{-1}$. The > 0.4 TeV integrated fluxes were $4.64 \pm 0.42 \times 10^{-11} \text{ ph cm}^{-2} \text{s}^{-1}$, $3.72 \pm 0.33 \times 10^{-11} \text{ TeV cm}^{-2} \text{s}^{-1}$, and $5.83 \pm 0.52 \times 10^{-11} \text{ erg cm}^{-2} \text{s}^{-1}$ (all values

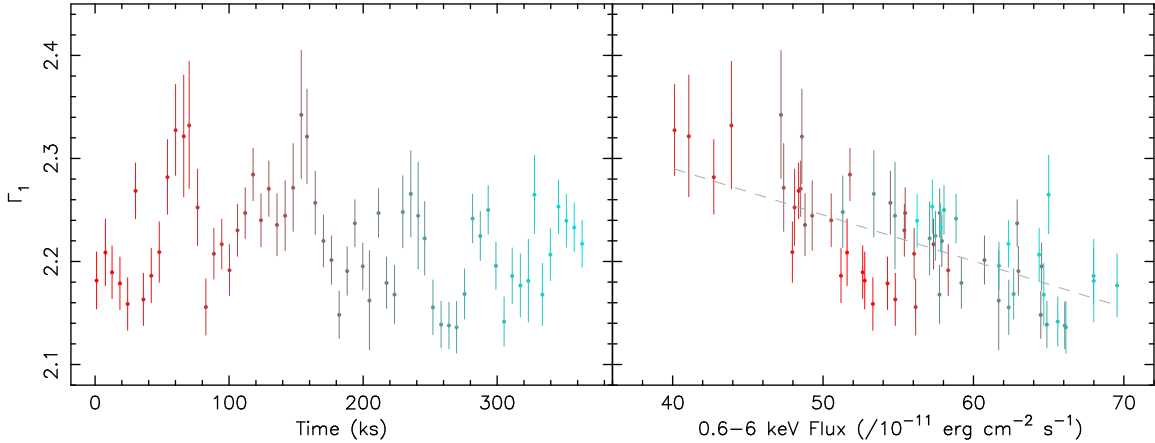


Figure 8. Results from the time-resolved spectral fits using the broken power-law model, with E_{break} frozen at 4.4 keV and Γ_2 fixed to $\Gamma_1 + 0.49$, where Γ_1 and Γ_2 denote the photon indices below and above the break energy, respectively. The left and right panels show Γ_1 as a function of time and flux, respectively; levels of red/cyan colour indicate points closer to the beginning/end of the observation. Time zero is the same as in Fig. 1. The dashed grey line is the best-fitting linear relation.

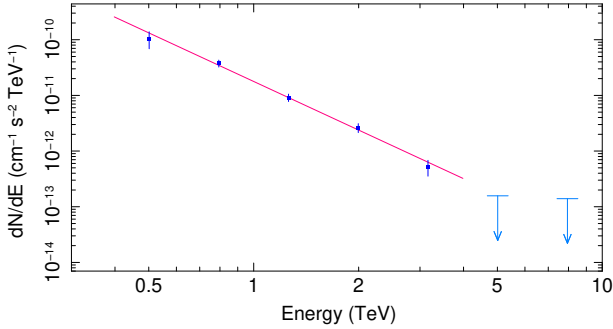


Figure 9. FACT TeV spectrum covering 2019 January 10–14. The red line is the best least-squares fit to the 0.4–4.0 TeV bins. These data were not corrected for EBL extinction.

here are for data not yet corrected for extragalactic background light extinction). We also extracted spectra for individual nightly bins to check for inter-night variability but found no significant evidence for it, so these nightly spectra are not discussed further.

Finally, in preparation for incorporating the FACT data on to the SED, we corrected νF_ν data points for extragalactic background light (EBL) extinction; we followed the prescription of Franceschini, Rodighiero, & Vaccari (2008), which increased flux density at 0.5 and 3.2 TeV (the midpoints of the lowest- and highest-energy bins with detections) by 14 and 60 per cent respectively.

7 SED CONSTRUCTION AND MODELING

We form the SED by combining the time-averaged B , V , R , and I flux densities, the best-fitting broken power-law fit to the time-averaged X-ray spectrum, the best fit to the time-averaged TeV spectrum, and the best-fitting power-law model to the *Fermi*-LAT spectrum. We also included the concurrent *Fermi*-LAT spectrum from the four-day period MJD 58493–7: we applied a power-law fit over the 0.1–8 GeV range, finding $\Gamma = 1.64 \pm 0.22$ and an integrated photon flux density of $1.11 \pm 0.36 \times 10^{-7}$ ph cm $^{-2}$ s $^{-1}$. We also included 15–50 keV data from *Swift*’s Burst Alert Transient (BAT) Hard X-

ray Transient Monitor program¹⁰ (Krimm et al. 2013) for a 30-day period centered on our campaign. One-day-binned count rate light curves were downloaded, binned to 30 days, and converted to flux based on the spectrum obtained in the 105 month BAT survey¹¹ (Oh et al. 2018): $F_{15-50} = 2.09 \pm 0.80 \times 10^{-10}$ erg cm $^{-2}$ s $^{-1}$. The resulting SED is plotted in Fig. 10.

The SED of Mkn 421 has been fitted with a family of one-zone leptonic models calculated with the BLAZAR code (Moderski, Sikora, & Błażejowski 2003). The code solves a kinetic equation for the energy distribution of electrons, including injection of a broken power-law distribution, as well as adiabatic and radiative losses (including synchrotron and synchrotron self Compton (SSC) mechanisms) along a conical jet. In Fig. 10 and Table 6, we present four SED models that differ by two key parameters: the jet bulk Lorentz factor Γ_j and the co-moving magnetic field strength B . These models have been fitted tightly to the X-ray spectrum observed by the *AstroSAT* and to the VHE gamma ray spectrum observed by the FACT, they have also been constrained by the optical flux density and colour. The injected electron energy distribution has been modeled as a broken power-law with two power-law sections: $N(\gamma) \propto \gamma^{-p_1}$ for $1 < \gamma < \gamma_{\text{br}}$, and $N(\gamma) \propto \gamma^{-p_2}$ for $\gamma_{\text{br}} < \gamma < \gamma_{\text{max}}$. We fixed the low-energy index at $p_1 = 2$, which determines the hardness of the synchrotron component in the optical band and of the SSC component in the HE gamma ray (*Fermi*) band. The high-energy index p_2 has been tuned for each model to match the *AstroSAT* and FACT spectra. The value of γ_{br} determines a proper connection of the optical and X-ray data by the synchrotron component. The VHE flux level is determined mainly by the distance r of the emitting region from the jet base, which in turn determines the lateral jet radius $R_j = r\theta_j$, where $\theta_j = 0.2/\Gamma_j$ is the jet half-opening angle (assuming a conical geometry). A larger emitting region results in a lower Compton dominance $L_{\text{SSC}}/L_{\text{syn}}$.

We have considered two values of the bulk Lorentz factor motivated by previous studies: $\Gamma_j = 25$ and $\Gamma_j = 12.5$. Given a value of Γ_j , the co-moving magnetic field strength B determines the level of HE gamma-ray emission (which scales roughly as $\propto B^{2/3}$), which is poorly constrained by the *Fermi*/LAT measurement

¹⁰ <https://swift.gsfc.nasa.gov/results/transients/>

¹¹ <https://swift.gsfc.nasa.gov/results/bs105mon/>

Table 6. Parameters of three SED models: Γ_j is the jet bulk Lorentz factor; $\theta_j = 0.2/\Gamma_j$ is the jet half-opening angle; $\theta_{\text{obs}} = \theta_j$, the jet viewing angle; $\delta = [\Gamma_j(1 - \beta_j \cos \theta_{\text{obs}})]^{-1}$ is the Doppler factor, with $\beta_j = (1 - 1/\Gamma_j^2)^{1/2}$, the jet bulk speed normalized to c ; r is the distance scale of the emitting region along a conical jet; $t_{\text{var}} = (1+z)R_j/\delta c$, the expected variability time-scale, with $R_j = r\theta_j$, the jet radius; and $p_1, p_2, \gamma_{\text{br}}, \gamma_{\text{max}}$ are parameters of the broken power-law electron energy distribution $N(\gamma) \propto \gamma^{-p_1}$ for $1 < \gamma < \gamma_{\text{br}}$ and $N(\gamma) \propto \gamma^{-p_2}$ for $\gamma_{\text{br}} < \gamma < \gamma_{\text{max}}$. Also reported are estimates of the jet power contained in the magnetic fields (L_B), the electrons (L_e), and the protons (L_p , one cold proton per electron).

Γ_j	25	25	25
B [G]	0.3	0.6	1.2
$\theta_j = \theta_{\text{obs}}$	0.008	0.008	0.008
δ	48	48	48
r [pc]	0.052	0.023	0.010
t_{var} [h]	0.25	0.11	0.05
p_1	2.0	2.0	2.0
p_2	2.85	2.8	2.8
$\gamma_{\text{br}} [\times 10^4]$	4.6	3.6	3.2
$\gamma_{\text{max}} [\times 10^6]$	3.0	3.0	3.0
$\log L_B$ [erg s $^{-1}$]	41.5	41.5	41.3
$\log L_e$ [erg s $^{-1}$]	43.1	43.0	42.8
$\log L_p$ [erg s $^{-1}$]	45.3	45.2	45.1

simultaneous with the *AstroSAT* campaign. Optimum levels of HE flux were obtained for $B = 0.6$ G with $\Gamma_j = 25$, and for $B = 0.3$ G with $\Gamma_j = 12.5$. Mild cooling breaks manifest themselves in these SED models; analytical estimates of cooling breaks can be obtained as follows: We estimate the associated electron Lorentz factor $\gamma_{\text{cool}} \simeq (m_e c^2 / \sigma_T)(\Gamma_j / (u_B r))$, following e.g., [Moderski, Sikora, & Błażejowski \(2003\)](#); the corresponding energy rollover in the SED is near $\sim 2 \times 10^{-8} \delta B [\text{G}] \gamma_{\text{cool}}^2 / (1+z)$ eV. Here, $\delta = [\Gamma_j(1 - \beta_j \cos \theta_{\text{obs}})]^{-1}$, the Doppler factor; $\theta_{\text{obs}} = \theta_j$, the jet viewing angle; $\beta_j = (1 - 1/\Gamma_j^2)^{1/2}$, the jet bulk speed normalized to c ; and $u_B = B^2/8\pi$ is the magnetic energy density. In the case of $\Gamma_j = 12.5$, a cooling rollover forms in the EUV band (~ 60 eV), resulting in a slight deficiency in the soft X-ray flux. For $\Gamma_j = 25$, values of γ_{cool} span $\sim 2 \times 10^4 - 5 \times 10^4$, with a cooling rollover near $\sim 0.3 - 0.8$ keV, but this rollover is very mild; spectral curvature in the X-ray band is dominated by a break in the electron energy distribution. Our models do not attempt to reproduce the sharp break in the hard X-ray band suggested by the best-fitting model to the *AstroSAT* data. We have adopted a maximum electron energy fixed at $\gamma_{\text{max}} = 3 \times 10^6$ in order to produce enough VHE emission. This results in the synchrotron components extending almost to the MeV band. Results for models with $\Gamma_j = 25$ are listed in Table 6. In Table 6, we report the expected variability time-scale $t_{\text{var}} = (1+z)R_j/\delta c$. The values of t_{var} range from 0.11 hr in the $\Gamma_j = 25$ case to 1.3 hr in the $\Gamma_j = 12.5$ case.

We also report three components of the predicted jet power contained in the magnetic fields, electrons and protons, assuming one cold proton for each electron (alternatively, assuming the presence of electron-positron pairs would reduce the predicted proton jet power, e.g., [Madejski et al. 2016](#)). We find very consistent results with $L_B \ll L_e \ll L_p$. The reason for this consistency is that the mean electron energy is determined mainly by the low-energy part of their distribution, which has been assumed to be fixed. The low energetic contribution of magnetic fields suggests a matter-dominated jet, which is a typical result for BL Lac type objects ([Tavecchio & Ghisellini 2016](#)).

8 DISCUSSION

8.1 Basic constraints from continuum variability

We conducted a 4-day contemporaneous campaign in X-ray, TeV, and optical bands on the HBL MkN 421 to explore its short-term variability properties. One of our campaign's strengths is the energy-resolved X-ray light curves from *AstroSAT* SXT, allowing us to examine X-ray variability on time-scales down to a few ks. The campaign caught four small flares in the X-ray band, each lasting roughly 50–100 ks.

An observed variability timescale can be used to infer an upper limit estimate for the size R of the emission region in the co-moving frame based on light travel time, and ignoring contributions from dynamic processes, via $R < ct_{\text{var}}\delta(1+z)^{-1}$. We first consider t_{var} to be the fastest observed variability time-scale. During our observation, the source X-ray flux increased by 22 per cent in six orbits (35.0 ks) in the 0.6–0.8 keV band (starting roughly 60 ks after the start of the *AstroSat* observation), and it increased by 82 per cent in two orbits (11.7 ks) in the 3–7 keV band (starting at roughly 70 ks after the start). Adopting $\delta = 25$ hereafter, a value consistent with the range derived from various SED fits (e.g., [Maraschi et al. 1999](#); [Abdo et al. 2011](#); [Aleksić et al. 2015a,b](#); [Acciari et al. 2020](#)) or rapid TeV variability ([Celotti, Fabian, & Rees 1998](#)), these values of t_{var} yield $R < 3 \times 10^{16}$ cm and $R < 8 \times 10^{15}$ cm for the 0.6–0.8 keV and 3–7 keV bands, respectively. Using a value of black hole mass $M_{\text{BH}} = 1.9 \times 10^8 M_\odot$ ([Woo & Urry 2002](#)), $1 R_g = 2.9 \times 10^{13}$ cm, and thus $R < 1000 R_g$ or $R < 300 R_g$ for the 0.6–0.8 or 3–7 keV bands, respectively. Alternatively, one can use the full duration of the flares as the variability time-scale, neglecting blending between successive flares. Using the same start/stop times as defined in §3.2 (Table 3), the average start-to-stop flare duration is 73 ks in the 0.6–0.8 keV band and 69 ks in the 3–7 keV band. Using these as t_{var} yields $R < 5 \times 10^{16}$ cm $\sim 1800 R_g$.

A scenario in which only cooling dominates the variability is excluded: we would expect relatively higher-energy X-ray bands to fall more quickly, but as is apparent from Fig. 1, all bands fall at roughly similar rates.

We can estimate the co-moving magnetic field strength B based on observed X-ray flux decays, and constraining the synchrotron cooling time-scale to be shorter than the fastest variability time-scale. The fastest observed decay time in the X-rays is in the 3–7 keV band, over 17.5 ks (3 orbits). We start from the synchrotron power emitted ([Rybicki & Lightman 1979](#)), $P_{\text{syn}} = \frac{4}{3} \sigma_T c \beta^2 \gamma^2 u_B$, where $u_B = B^2/8\pi$ is the magnetic energy density, σ_T is the Thomson cross section, 6.7×10^{-25} cm 2 , γ is the Lorentz factor for the emitting electron, $\beta \equiv v/c \sim 1$ for ultra-relativistic electrons. We define the synchrotron cooling time as $\tau_{\text{synch}} \equiv (\text{electron energy})/(\text{synchrotron power loss}) = \gamma m_e c^2 / P_{\text{syn}}$, or

$$\tau_{\text{synch}} = \frac{3m_e c}{4\sigma_T \gamma u_B} \quad (2)$$

Note this refers to the cooling time in the rest frame; the observed cooling time-scale $\tau_{\text{synch,obs}} = \tau_{\text{synch}}(1+z)\delta^{-1}$. Solving for B , we obtain

$$B = \sqrt{\frac{6\pi(1+z)m_e c}{\sigma_T \delta \gamma \tau_{\text{synch,obs}}}} \quad (3)$$

To solve for γ , we use the expression for the peak synchrotron emission energy produced by monoenergetic electrons with Lorentz factor γ and averaged over magnetic pitch angle from [Nalewajko et](#)

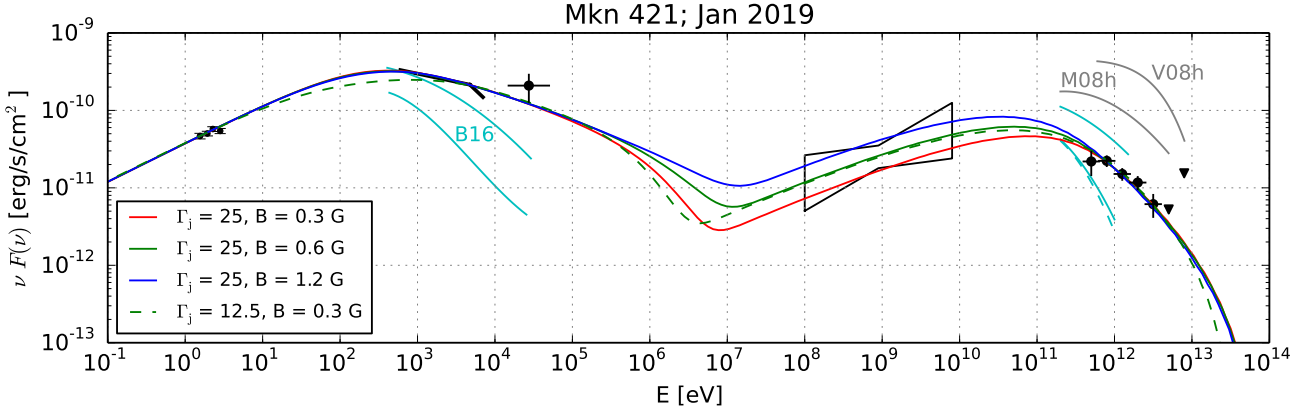


Figure 10. Spectral energy distribution (SED) of Mkn 421 during our campaign. The results of WEBT, *AstroSat*, and FACT observations in January 2019 are shown in black symbols; also included are a concurrent *Fermi*-LAT spectrum and a *Swift*-BAT flux point. For comparison, the X-ray and VHE measurements of Mkn 421 in two flux states selected from Baloković et al. (2016, their Fig. 13, MJD 56302 and 56335) are shown with cyan lines. The gray lines show the high VHE states measured by MAGIC and VERITAS in their 2008 campaigns (Aleksić et al. 2012; Acciari et al. 2011). The broad-band lines show one-zone synchrotron+SSC leptonic models matched to the optical, X-ray and VHE data.

al. (2011),

$$E_{\text{syn}} = 2 \times 10^{-8} \delta B \gamma^2 (1+z)^{-1} \text{ eV} \quad (4)$$

Rearranging to solve for B , we obtain

$$B = \left(\frac{6\pi m_e c}{\sigma_T \tau_{\text{synch,obs}}} \right)^{2/3} \left(\frac{(2 \times 10^{-8} \text{ eV})(1+z)}{\delta E_{\text{syn}}} \right)^{1/3} \text{ G} \quad (5)$$

Using $E_{\text{syn}}=5000$ eV, and using the average 3–7 keV flare duration as an upper limit to $\tau_{\text{synch,obs}}$, we obtain a lower limit on the co-moving magnetic field: $B > \sim 0.08 \delta^{-1/3}$ G. Defining $\delta_{25} \equiv \delta/25$, therefore $\delta^{-1/3} = 0.3 \times \delta_{25}^{-1/3}$, and finally $B > \sim 0.02 \delta_{25}^{-1/3}$ G.

8.2 Constraints from intra-X-ray cross-correlations

During the first two X-ray flares observed in our campaign, relatively harder bands increase in flux later than softer bands; it can be seen from Fig. 1 that during the first two minima the 0.6–0.8 keV band begins to increase while the 3–7 keV band is still decreasing. These trends drive a soft-to-hard lag between the 0.6–0.8 keV band and the other bands. However, the harder bands increase more rapidly, and even peak earlier than the softer bands. These observations are consistent with the notion that when there is a dissipation event, it develops at relatively lower energies first, but works more effectively towards harder bands later on. In contrast, the third and fourth flares are more time-symmetric across all X-ray sub-bands.

The fact that most bands are well-correlated at lags consistent with zero supports emission originating in homogeneous regions where particles emitting high- and low-energy photons are co-spatial. It could also indicate that cooling and acceleration time-scales are overall roughly equal, particularly for flares 3 and 4. (Having $\tau_{\text{cool}} \sim \tau_{\text{accel}}$ is reasonable to expect given that the X-ray band in HBLs corresponds to the high-energy regime of synchrotron emission; Kirk, Reiger, & Mastichiadis 1998).

However, cross-correlations do not cleanly distinguish between flares peaking first at harder energies versus acceleration impacting the softer bands first. Both processes seem to be present during flares 1 and 2; the combination of processes can lead to overall observed lags near zero.

Nonetheless, given that we do measure a net soft-to-hard lag across flares 1 and 2, we can explore further the notion that acceleration processes impact relatively lower energies first, so that energized electrons appear at low energies first and gradually build up towards higher energies (Georganopoulos & Marscher 1998).

Under the assumption that cooling and acceleration time-scales are roughly equal, the soft-to-hard lag indicates acceleration occurring at lower electron energies first and progressively later to higher energies following Eqn. 9 of Zhang et al. (2002):

$$B \delta \xi_{\text{acc}}^{-2/3} = 0.21 (1+z) E_{\text{hi}}^{1/3} \left[\frac{1 - (E_{\text{lo}}/E_{\text{hi}})^{1/2}}{\tau_{\text{lag}}} \right]^{2/3} \text{ G} \quad (6)$$

where B is the co-moving magnetic field strength in Gauss, and τ_{lag} is the value of the observed soft-to-hard delay from E_{lo} to E_{hi} in seconds (best-fitting value of 4600). Using the pitch angle-averaged photon energy as in Eq. 4 introduces a mere 10 per cent difference (one replaces the constant 0.21 with 0.19). We adopt 0.7 and 2 keV for E_{lo} and E_{hi} , respectively, and again adopt $\delta_{25} \equiv \delta/25$.

As discussed in §5.2 of Zhang et al. (2002), the value of the acceleration parameter ξ_{acc} is not clear; we define $\xi_{\text{acc},5} \equiv \xi_{\text{acc}}/10^5$. We obtain $B \sim 0.05 \delta_{25}^{-1} \xi_{\text{acc},5}^{2/3}$ G. However, given that the observed lag has likely been diluted by contemporaneous hard-to-soft processes, this derived estimate of B can be treated as a lower limit.

Hard-to-soft lags are generally expected in the context of the electron population becoming softer due to synchrotron radiative losses; if synchrotron losses dominate, then the magnitude of the hard-to-soft lag can constrain τ_{cool} , and thus B , following e.g., Chiappetti et al. (1999, their eqn. 1).

In this campaign, we find only upper limits on hard-to-soft lags; the highest upper limit was 4.4 ks (ICF centroid, second half only, 3–7 keV band leading 0.6–0.8 keV), which implies a lower limit of $B \delta^{1/3} \gtrsim 0.7$ G following Chiappetti et al. (1999), or $B \delta_{25}^{1/3} \gtrsim 0.2$ G.

8.3 Constraints from energy-dependent variability amplitudes

We observed fractional variability amplitude F_{var} to increase with energy across the synchrotron hump, following a best-fitting relation $F_{\text{var}} \propto E^{+0.20}$ across both the X-ray band and from optical/NIR to the X-rays, and consistent with previous results for Mkn 421.

An observed energy dependence for F_{var} argues against variability being due predominantly to changes in magnetic field strength or size of emission region or due to changes in Doppler factor δ (e.g., from viewing angle). That is, the observed flares' being produced by rapid precession of a single emission component about the jet axis is unlikely, despite the roughly similar amplitudes of all four flares. The observed energy dependence instead supports variability being dominated by acceleration/cooling.

An alternate possibility is that the occurrence of relatively lower fractional variability towards lower energies could be consistent with an additional constant or less-variable emission term: assuming a variability process that yields the same variance across a waveband, increasing the mean by a certain factor would reduce F_{var} by that factor. An emission component whose integrated 0.6–0.8 keV flux is twice that in the 3–7 keV band would have values of F_{var} in those bands differing by 2, as observed. Conjecturally extrapolating to the optical band, one requires an emission component with flux integrated across a given optical filter ~ 8 times that at 3–7 keV. However, for the sake of exploring models in a straightforward manner, we ignore such a putative term and assume that all observed emission is from variable components of the jet.

We can consider a context in which the observed synchrotron emission is the superposition of radiation from a large number of distinct individually-emitting cells. We follow the turbulent cells model of [Marscher & Jorstad \(2010\)](#), in which cells have a similar size, and their EED widths are distributed such that those cells capable of emitting at relatively higher energies are present in relatively smaller volume filling factors. More specifically, we consider a phenomenological toy model in which each cell emits a spectrum represented by a power-law with photon index $\Gamma_0 = 1.3$, modified with a high-energy exponential rollover at energy E_{cut} . As a starting assumption, we assume that this power-law extrapolates from X-rays (10 keV) down to the optical/IR band (1 eV). The number density of cells that have a certain value of E_{cut} follows a power-law distribution as $dN/dE_{\text{cut}} \propto E_{\text{cut}}^{-\alpha_0}$. We consider a model set-up with N such cells; typically of order 30000 cells are needed for numerical convergence and to yield variability amplitudes consistent with our observations. We assume that all cells have the same size, and are all subject to identical amounts of radiative cooling and Doppler beaming.

We simulate light curves with 100 time steps, and consisting of multiple time-symmetric flares: exponentially-rising and -decaying flares are generated following Eqn. 1, with the time between successive flares chosen from uniform distributions. For simplicity, rise and fall times are set equal to each other at all energies and to 1/100 of the light curve duration. We simulate light curves in 20 energy sub-bands logarithmically spaced from 1 eV to 10 keV. For simplicity, we neglect the energy-dependency of synchrotron cooling times. An example set of energy-dependent light curves is plotted in Fig. 11. We sum the emission in each sub-band, measure F_{var} from each of the 20 summed sub-band light curves, and fit a power-law model to $F_{\text{var}}(E) \propto E^{-\alpha_{\text{Fv}}}$ as plotted in the second panel of Fig. 11. We tested values of α_0 ranging from 1.05 to above 2.0 in steps of 0.05, though solutions tended to not converge above $\alpha_0 = 2.0$. We repeated this procedure 100 times to build up distributions of

α_{Fv} for each value of α_0 tested. As plotted in Fig. 12, we find that $\alpha_0 = 1.35^{+0.08}_{-0.07}$ yields results consistent with the observed value of $\alpha_{\text{Fv}} = 0.20 \pm 0.01$.

This is admittedly a simple toy model, and there is room for additional development; one could additionally consider variations in source size, Doppler beaming, radiative cooling, and in dN/dE_{cut} . Such considerations could potentially lead to the model output broadband energy spectrum having more curvature at 0.1–1 keV, thus more closely matching the broadband shape of the observed SED. However, we leave such detailed development for future papers.

9 CONCLUSIONS

We have presented results obtained from a 4-day coordinated multi-wavelength campaign on the HBL Mkn 421 in January 2019, conducted to better study this blazar's short time-scale variability properties and gain insight into the properties of the emitting regions.

We gathered continuous X-ray monitoring with *AstroSat* SXT and LAXPC, tracking full- and sub-band variability down to satellite orbital time-scales (98 minutes). The FACT telescope provided nightly TeV monitoring, with up to ~ 22 ks (~ 6 hours) of data taken each night. The Whole Earth Blazar Telescope consortium (most notably the EPT telescope on La Palma) provided contemporaneous B-, V-, R-, and I-band photometric monitoring during our campaign.

Our primary findings are summarized as follows:

- Our campaign caught four modest X-ray flares ($\sim 20 - 60$ per cent flux increases/decreases, depending on sub-band energy), each lasting on time-scales of roughly \lesssim a day. However, the source exhibited minimal night-to-night variability in any energy range, precluding any meaningful interband correlation analysis from this campaign.
- We studied energy-dependent variability within the X-ray band using *AstroSat* SXT. During the first two flares, relatively harder X-rays are associated with shorter rise times and longer decay times, while relatively softer X-rays are associated with more symmetric flares. The relatively harder bands increase in flux later and faster compared to the softer X-rays, leading to an observed soft-to-hard lag of an average of 4.6 ± 2.6 ks from the 0.6–0.8 keV sub-band to the harder sub-bands during the first two flares (though there likely co-exist contemporaneous hard-to-soft and soft-to-hard emission processes). The third and fourth flares are more time-symmetric across all X-ray sub-bands.
- Continuum flux variability amplitudes increase monotonically with energy across both the X-ray band ($F_{\text{var}} \propto E^{0.26 \pm 0.01}$) and across the synchrotron hump from NIR/optical to X-rays ($F_{\text{var}} \propto E^{0.20 \pm 0.01}$), consistent with previous measurements for Mkn 421 and for other HBL blazars. We explain this behaviour in the context of a simple toy model in which the observed synchrotron emission originates in a large number of individual cells whose EEDs are distributed such that relatively higher energy-emitting cells occupy relatively smaller volumes. Each cell emits a power-law spectrum across the NIR/optical-to-X-ray band, but with an exponential cut-off, and the distribution of cutoffs E_{cut} follows a power law as $dN/dE_{\text{cut}} \propto E_{\text{cut}}^{-\alpha_0}$. Simulations of sub-band light curves that follow such a distribution yields the result that a power-law index of $\alpha_0 = 1.35^{+0.08}_{-0.07}$ yields results an energy-dependent variability behaviour consistent that observed during our campaign.
- We fit the time-averaged X-ray spectrum, composed of 0.6–7 keV SXT and 3–7 keV LAXPC data. A mildly broken power law

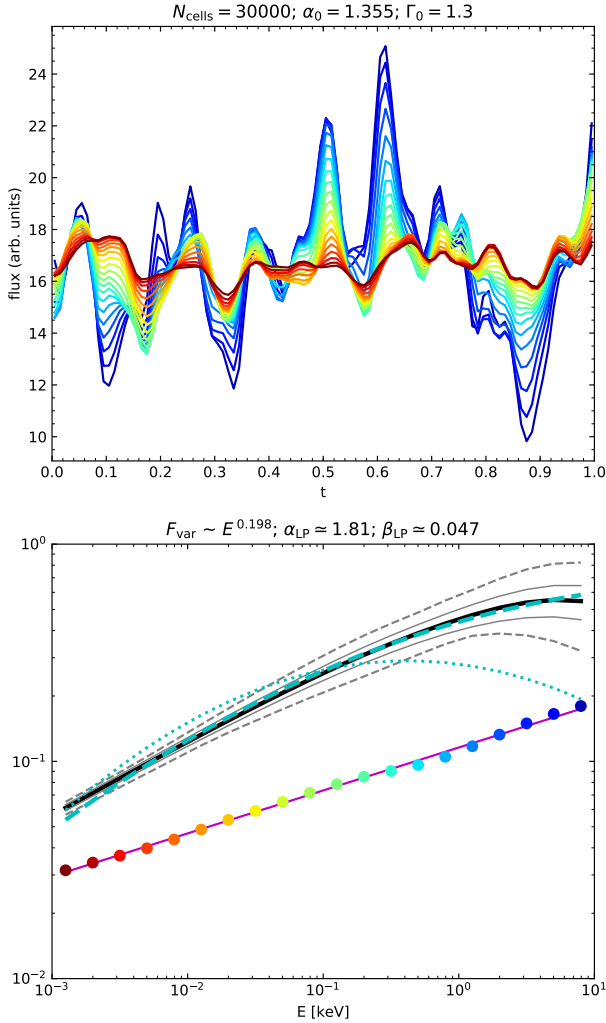


Figure 11. Results from one run of our toy cell model based on having a large number of independent emission sources, with emission characterized by a power-law distribution of exponential cut-off energies following $dN/dE_{\text{cut}} \propto E_{\text{cut}}^{-\alpha_0}$. The top panel shows a simulated set of 20 energy-dependent light curves from optical (dark red; down to 1 eV) to X-ray (dark blue; up to 10 keV) energies, all normalized to the same mean. In this particular run, $\alpha_0 = 1.355$. The bottom panel shows the variability amplitudes F_{var} , with colours corresponding to the light curves displayed in the left panel. The solid magenta line shows the best-fitting power-law trend of $F_{\text{var}} \propto E^{0.198}$. The solid black line shows the mean (averaged over time) νF_{ν} SED (in arbitrary units) obtained in the simulation, the solid gray lines indicate the $\pm 1\sigma$ confidence limits, and the dashed gray lines indicate the minimum and maximum values. The dashed cyan line is the best log-parabola model (with parameters $\alpha_{\text{LP}} \approx 1.81$ and $\beta_{\text{LP}} \approx 0.047$) fitted to the solid black line. The dotted cyan line is the log-parabola model that matches the observed optical-to-X-ray SED of Mkn 421 (with arbitrary normalization).

(with photon index $\Gamma_1 = 2.20 \pm 0.01$ below a break energy of $5.0^{+0.2}_{-0.2}$ keV breaking to $\Gamma_2 = 2.73^{+0.23}_{-0.13}$ above it) is a superior fit than an unbroken power-law. Time-resolved fits to orbitally-binned data using this broken power-law model, and with Γ_2 fixed to $\Gamma_1 + 0.49$ yields the usual qualitative hardening-when-brightening behaviour common to blazar emission. No obvious signs of hysteresis in the Γ_1 -flux plane were observed during our campaign; no signs of differing spectral variability behaviour between the four X-ray flares was evident.

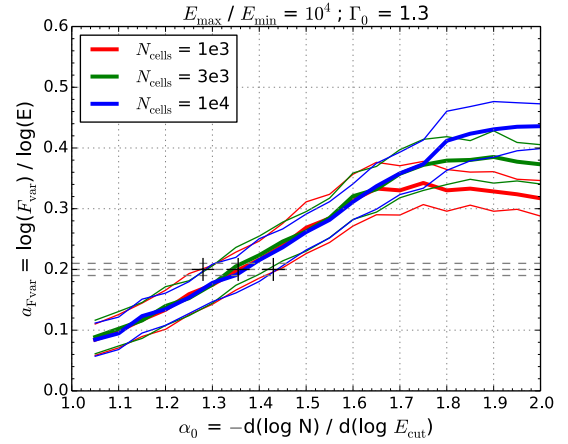


Figure 12. Results of simulations detailing the behaviour of a_{Fvar} , the power-law index of variability amplitude as function of observed photon energy, as a function of α_0 , which quantifies the distribution of high-energy spectral cutoffs. Red, green, and blue lines indicate simulations with 3000, 10000, and 30000 cells, respectively. For each value of α_0 , the thick and thin solid lines indicate the mean and standard deviations, respectively, of 100 simulations. Values of α_0 between 1.28 and 1.43 yield values of a_{Fvar} consistent with the best-fitting observed value of a_{Fvar} .

- We constructed the broadband SED for this campaign, combining AstroSat, optical/NIR flux densities, FACT TeV flux densities, and contemporaneous *Fermi* LAT data. A standard one-zone leptonic model including synchrotron and SSC emission fits the overall SED well for a co-moving magnetic field strength $B \sim 0.3\delta_{25}$ G. The model fits imply a low magnetic power and a matter-dominated jet, as is typically found for BL Lac type objects.

- We have derived multiple constraints on the co-moving magnetic field strength: $B > \sim 0.02\delta_{25}^{-1/3}$ G by requiring the synchrotron cooling time-scale to be shorter than the typical flare time-scale (§8.1); $B > \sim 0.05\delta_{25}^{-1}\xi_{\text{acc},5}^{2/3}$ G from observed soft-to-hard intra-X-ray lags (§8.2); and $B > 0.2\delta_{25}^{-1/3}$ G based on upper limits to hard-to-soft lags (§8.2). These limits are consistent with the estimate of $B \sim 0.3\delta_{25}$ G obtained from SED model fits (§7).

ACKNOWLEDGEMENTS

A.G.M. and S.K. acknowledge partial support from Narodowe Centrum Nauki (NCN) grants 2016/23/B/ST9/03123 and 2018/31/G/ST9/03224. A.G.M. also acknowledges support from NCN grant 2019/35/B/ST9/03944. K.N. was supported by NCN grant 2015/18/E/ST9/00580. G.B. acknowledges support from NCN grant 2017/26/D/ST9/01178. S.Z. acknowledges support from NCN grant 2018/29/B/ST9/01793. E.B. acknowledges support from DGAPA-UNAM grant IN113320. S.M. Hu acknowledges the sup-

port from the Natural Science Foundation of China under grant No. 11873035. K.M. acknowledges support from JSPS KAKENHI grant number 19K03930.

This publication uses the data from the AstroSat mission of the Indian Space Research Organisation (ISRO), archived at the Indian Space Science Data Centre (ISSDC). This work has used the data from the Soft X-ray Telescope (SXT) developed at TIFR, Mumbai, and the SXT POC at TIFR is thanked for verifying and releasing the data via the ISSDC data archive and providing the necessary software tools.

This research has made use of ISIS functions (ISISscripts) provided by ECAP/Remeis observatory and MIT (<http://www.sternwarte.uni-erlangen.de/isis/>).

This research has made use of data and/or software provided by the High Energy Astrophysics Science Archive Research Center (HEASARC), which is a service of the Astrophysics Science Division at NASA/GSFC.

The important contributions from ETH Zurich grants ETH-10.08-2 and ETH-27.12-1 as well as the funding by the Swiss SNF and the German BMBF (Verbundforschung Astro- und Astroteilchenphysik) and HAP (Helmoltz Alliance for Astroparticle Physics) are gratefully acknowledged. Part of this work is supported by Deutsche Forschungsgemeinschaft (DFG) within the Collaborative Research Center SFB 876 "Providing Information by Resource-Constrained Analysis", project C3. We are thankful for the very valuable contributions from E. Lorenz, D. Renker and G. Viertel during the early phase of the project. We thank the Instituto de Astrofísica de Canarias for allowing us to operate the telescope at the Observatorio del Roque de los Muchachos in La Palma, the Max-Planck-Institut für Physik for providing us with the mount of the former HEGRA CT3 telescope, and the MAGIC collaboration for their support.

This research was partially supported by the Bulgarian National Science Fund of the Ministry of Education and Science under grants DN 18-10/2017, DN 18-13/2017, KP-06-H28/3 (2018), KP-06-H38/4 (2019) and KP-06-KITAJ/2 (2020).

Part of the photometric data included in this work were collected during the photometric monitoring observations with the robotic and remotely controlled observatory at the University of Athens Observatory (UOAO; [Gazeas 2016](#)).

The authors (Dr. J.R. Webb) are honored to be permitted to conduct astronomical research on Iolkam Du'ag (Kitt Peak), a mountain with particular significance to the Tohono O'odham Nation.

This work is partially based on observations collected at the Observatorio Astronómico Nacional at San Pedro Mártir Baja California, Mexico.

DATA AVAILABILITY STATEMENT

The data underlying this article will be shared on reasonable request to the corresponding author.

References

Abeysekara A.U., Archambault S., Archer A., et al., 2017, *ApJ*, 834, 2
 Acciari V., Aliu E., Arlen T., et al., 2011, *ApJ*, 738, 25
 Acciari V., Ansoldi S., Antonelli L.A., et al., 2020, *ApJS*, 248, 29
 Abdo A.A., Ackermann M., Agudo I., et al., 2010, *ApJ*, 716, 30
 Abdo A.A., Ackermann M., Ajello M., et al., 2011, *ApJ*, 736, 131
 Acero F., et al. 2015, *ApJS*, 218, 23
 Ackermann M., et al., 2016, *ApJ*, 824, L20

Agrawal P.C., Yadav J.S., Antia H.M., et al., 2017, *JApA*, 38, 30
 Aharonian F., Akhperjanian A.G., Bazer-Bachi A.R., et al., 2007, *ApJ*, 664, L71
 Ahnen M.L., Ansoldi S., Antonelli L.A., et al., 2016, *A&A*, 593, A91
 Akaike H., 1973, in Petrov B.N., Caski F., eds., *Proc. of the Second International Symposium on Information Theory*, p. 267–281, Budapest: Akademiai Kiado
 Albert J., Aliu E., Anderhub H., et al., 2007, *ApJ*, 663, 125
 Aleksić J., Alvarez E.A., Antonelli L.A., et al., 2012, *A&A*, 542, A100
 Aleksić J., Ansoldi S., Antonelli L.A., et al., 2015a, *A&A*, 576, A126
 Aleksić J., Ansoldi S., Antonelli L.A., et al., 2015b, *A&A*, 578, A22
 Alexander T., 1997, in Maoz D., Sternberg A., Leibowitz E.M., eds, *Astronomical Time Series*. Kluwer, Dordrecht, p. 163
 Alexander T., 2013, *arXiv e-prints*, arXiv:1302.1508
 Algeri S., van Dyk D.A., Conrad J., Anderson B., 2016, *J. Instrum*, 11, P2010A
 Amenomori M., Ayabe S., Cui S.W., et al., 2003, *ApJ*, 598, 242
 Anderhub H., Backes M., Biland A., et al., 2013, *JInst*, 8, P6008
 Antia H.M., Yadav J.S., Agrawal P.C., et al., 2017, *ApJS*, 231, 10
 Arbet-Engels A., Baack D., Balbo M., et al., 2021, *A&A*, 647, A88
 Atwood W.B., et al. 2009, *ApJ*, 697, 1071
 Baloković M., Paneque D., Madejski G., et al., 2016, *ApJ*, 819, 156
 Beck M., Arbet-Engels A., Baack D., et al., 2019, 36th International Cosmic Ray Conference (ICRC2019), held July 24th–August 1st, 2019 in Madison, WI, U.S.A. Online at <https://pos.sissa.it/cgi-bin/reader/conf.cgi?confid=358>, id.630
 Bessell M. S., Castelli F., Plez B., 1998, *A&A*, 333, 231
 Bhatta G., Dhital N., 2020, *ApJ*, 891, 120
 Bhatta G., Stawarz L., Ostrowski M., et al., 2016, *ApJ*, 831, 92
 Biland A., Bretz T., Buß J., et al., 2014, *Journal of Instrumentation*, 9, P10012
 Blandford R.D., Znajek R.L., 1977, *MNRAS*, 179, 433
 Blażejowski M., Blaylock G., Bond I.H., et al., *ApJ*, 630, 130
 Böttcher M., Dermer C., 2010, *ApJ*, 711, 445
 Böttcher M., Reimer A., Sweeney K., Prakash, A., 2013, *ApJ*, 768, 54
 Bretz T., 2019, *Aph*, 111, 72
 Bretz T., Dorner D., in Leroy C., Rancoita P., Barone M. et al., eds, *Astroparticle, particle and space physics, detectors and medical physics applications*. Proceedings of the 11th Conference. World Scientific Publishing Co. Pte. Ltd, Singapore, p. 681
 Cardelli J.A., Clayton G.C., Mathis J.S., 1989, *ApJ*, 345, 245
 Carnerero M., Raiteri C.M., Villata M., et al., 2017, *MNRAS*, 472, 3789
 Celotti A., Fabian A.C., Rees M.J., 1998, *MNRAS*, 293, 239
 Chatterjee R., Roychowdhury A., Chandra S., Sinha A., 2018, *ApJ*, 859, L21
 Chiappetti L., Maraschi L., Tavecchio F., et al., 1999, *ApJ*, 521, 552
 Cui W., 2004, *ApJ*, 605, 662
 De Vaucouleurs G., De Vaucouleurs A., Corwin Jr. H.G., Buta R.J., Paturel G., Fouque P., 1991, *Third Reference Catalogue of Bright Galaxies*, version 3.9, Springer: New York, NY (USA)
 Dorner D., Ahnen M.L., Bergmann M., et al., 2015, 2014 Fermi Symposium proceedings - eConf C14102.1, eprint arXiv:1502.02582
 Dorner D., Arbet-Engels A., Baack D., et al., 2019, 36th International Cosmic Ray Conference (ICRC2019), held July 24th–August 1st, 2019 in Madison, WI, U.S.A. Online at <https://pos.sissa.it/cgi-bin/reader/conf.cgi?confid=358>, id.665
 Edelson R., Griffiths G., Markowitz A., Sembay S., Turner M.J.L., Warwick R., 2001, *ApJ*, 554, 274
 Edelson R., Krolik J., 1988, *ApJ*, 333, 646
 Emmanoulopoulos D., McHardy I.M., & Papadakis I.E., 2013, *MNRAS*, 433, 907
 Fossati G., Buckley J.H., Bond I.H., et al., 2008, *ApJ*, 677, 906
 Fossati G., Celotti A., Chiaberge M., et al., 2000, *ApJ*, 541, 153
 Franceschini A., Rodighiero G., Vaccari M., 2008, *A&A*, 487, 837
 Gaskell C.M., Sparke L.S., 1986, *ApJ*, 305, 175
 Gazeas, K. 2016, *RMxAC*, 48, 22
 Georganopoulos M., Marscher A., 1998, *ApJ*, 506, 621
 Ghisellini G., Tavecchio F., Chiaberge M., 2005, *A&A*, 432, 401

- Giebels B., Dubus G., Khélifi B., 2007, *A&A*, 462, 29
- Hildebrand D., Ahnen M.L., Balbo M., et al., 2017, 35th International Cosmic Ray Conference. 10-20 July, 2017. Bexco, Busan, Korea, Proceedings of Science, Vol. 301. Online at <https://pos.sissa.it/cgi-bin/reader/conf.cgi?confid=301>, id.779
- Kataoka J., Takahashi T., Makino F., et al., 2000, *ApJ*, 528, 243
- Kirk J.G., F.M. Reiger, Mastichiadis A., 1998, *A&A*, 333, 452
- Krawczynski H., Coppi P.S., Aharonian F., 2002, *MNRAS*, 336, 721
- Krawczynski H., Coppi P.S., Maccarone T., Aharonian F., 2000, *A&A*, 353, 97
- Krawczynski H., Hughes S.B., Horan D., et al., 2004, *ApJ*, 601, 151
- Krimm H.A., Holland S.T., Corbet R.H.D., et al., 2013, *ApJS*, 209, 14
- Lichti G.G., Bottacini E., Ajello M., et al., 2008, *A&A*, 486, 721
- Madejski G., Nalewajko K., Madsen K.K., et al., 2016, *ApJ*, 831, 142
- Mahlke M., Bretz T., Adam J., et al., 2017, 35th International Cosmic Ray Conference. 10-20 July, 2017. Bexco, Busan, Korea, Proceedings of Science, Vol. 301. Online at <https://pos.sissa.it/cgi-bin/reader/conf.cgi?confid=301>, id.612
- Mannheim K., 1993, *A&A*, 269, 67
- Mannucci F., Basile F., Poggianti B.M., Cimatti A., Daddi E., Pozzetti L., Vanzi L., 2001, *MNRAS*, 326, 745
- Maraschi L., Fossati G., Tavecchio F., et al., 1999, *ApJ*, 526, L84
- Marscher A.P., Jorstad S.G., 2010, proc. of conference “Fermi meets Jansky – AGN in Radio and Gamma-Rays,” eds. Savolainen T., Ros E., Porcas R.W., & Zensus J.A., 2010 Jun, Bonn, Germany; arxiv: 1005.5551
- Mastichiadis A., Kirk J.G., 1997, *A&A*, 320, 19
- McGimsey B.Q., Miller H.R., Willamon R.M., 1976, *AJ*, 81, 750
- Moderski R., Sikora M., Błażejowski M., 2003, *A&A*, 406, 855
- Mücke A., Protheroe R., 2001, *Aph*, 15, 121
- Nalewajko K., Giannios D., Begelman M.C., Uzdensky D.A., Sikora M., 2011, *MNRAS*, 413, 333
- Nowak, M. A., Neilsen, J., Markoff, S. B., et al. 2012, *ApJ*, 759, 95
- Oh K., Koss M., Markwardt C.B., et al., 2018, *ApJS*, 235, 4
- Pian, E., 2002, *PASA*, 19, 29
- Peterson B.M., Wanders I., Horne K., et al., 1998, *PASP*, 110, 660
- Punch M., Akerlof C.W., Cawley M.F., et al., 1992, *Nature*, 358, 477
- Raiteri C.M., Villata M., Acosta-Pulido J.A., et al., 2017, *Nature*, 552, 374
- Ravasio M., Tagliaferri G., Ghisellini G., Tavecchio F., 2004, *A&A*, 424, 841
- Rebillot P.F., Badran H.M., Blaylock G., et al., 2006, *ApJ*, 641, 740
- Rybicki G.B., Lightman A.P., 1979, *Radiative Processes in Astrophysics*, New York: Wiley-Interscience
- Schleicher B., Arbet-Engels A., Baack D., et al., 2019, *Galaxies*, 7, 62
- Sembay S., Edelson R., Markowitz A., Griffiths R.G., Turner M.J.L., 2002, *ApJ*, 574, 634
- Sikora M., et al., 2005, *ApJ*, 625, 72
- Singh K. P., Stewart G. C., Westergaard N. J., Bhattacharayya S., Chandra S., Chitnis V. R., Dewangan G. C., et al., 2017, *JApA*, 38, 29. doi:10.1007/s12036-017-9448-7
- Singh K. P., Tandon S. N., Agrawal P. C., Antia H. M., Manchanda R. K., Yadav J. S., Seetha S., et al., 2014, *SPIE*, 9144, 91441S. doi:10.1117/12.2062667
- Sironi L., Petropoulou M., Giannios D., 2015, *MNRAS*, 450, 183
- Sugiura N., 1978, *Commun. Stat. – Theory Methods*, 7, 13
- Takahashi T., Tashiro M., Madejski G., et al., 1996, *ApJ*, 470, L89
- Takahashi T., Kataoka J., Madejski G., et al., 2000, *ApJ*, 542, L105
- Tanihata C., Urry C.M., Takahashi T., et al., 2001, *ApJ*, 563, 569
- Tavecchio F., Ghisellini G., 2016, *MNRAS*, 456, 2374
- Timmer J., König M., 1995, *A&A*, 300, 707
- Ulrich M.-H., Maraschi L., Urry C.M., *ARA&A*, 35, 445
- Urry C.M., Padovani P., 1995, *PASP*, 107, 803
- Vaughan S., 2005, *A&A*, 431, 391
- Vaughan S., Edelson R., Warwick R.S., Uttley P., 2003, *MNRAS*, 345, 1271
- Vaughan S., Uttley P., Markowitz A.G., Huppenkothen D., Middleton M.J., Alston W.N., Scargle J.D., Farr W.M., 2016, *MNRAS*, 461, 3145
- Villata M., Raiteri C.M., Kurtanidze O.M., et al., 2002, *A&A*, 390, 407
- Villata M., Raiteri C.M., Lanteri L., Sobrito G., Cavallone M., 1998, *A&AS*, 130, 305
- White R., Peterson B.M., 1994, *PASP*, 106, 879
- Willingale R., Starling R.L.C., Beardmore A.P., Tanvir N.R., O’Brien P.T., 2013, *MNRAS*, 431, 394
- Woo J.H., Urry C.M., 2002, *ApJ*, 579, 530
- Yadav J.S., Agrawal P.C., Antia H.M., et al., 2016, *Proc. SPIE*, 9905, 99051D
- Yan D., Zhang L., Yuan Q., et al., 2013, *ApJ*, 765, 122
- Zhang Y.H., Treves A., Celotti A., et al., 2002, *ApJ*, 572, 762
- Zola S., Kouprianov V., Reichart D.E., Bhatta G., Caton D.B., 2021, *RMxAC*, 53, 206

APPENDIX A: ASTROSAT SXT PERIDOGRAM MEASUREMENT

We measured the periodogram of the 1.4–1.9 keV SXT light curve; it had the highest count rate and thus lowest expected power due to Poisson noise. Following the method of [Vaughan \(2005\)](#), we first model the broadband continuum noise by fitting a power-law in log-log space to the red noise-dominated portion of the periodogram, excluding the candidate bump and those points above $\sim 6 \times 10^{-5}$ Hz dominated by Poisson noise.

Our best-fitting power-law slope is -1.96 ± 0.14 , and the best-fitting normalization (logarithm of power in units of $\text{rms}^2 \text{ Hz}^{-1}$ at 10^{-5} Hz) is 2.16 ± 0.21 . The candidate bump at $\sim 1.5 \times 10^{-5}$ Hz yields a value of the ratio I/P (where I denotes the periodogram power of the candidate signal and P denotes the value of the best-fitting continuum model) of 6.02 for our best-fitting model, but as low as only 3.74 considering the parameter uncertainties (the relative scarcity of sampled frequencies here means that the measured continuum level is not well constrained). Applying Eqn. 16 of [Vaughan \(2005\)](#) to take into account the “look elsewhere” effect ([Algeri et al. 2016](#)) given the number of independent frequencies sampled yields that the bump is inconsistent with being due to pure red noise at the 93.1 per cent confidence level for the best-fitting model, but merely the 48 per cent confidence level considering the parameter uncertainties.

In addition, caution must be applied here on multiple levels, particularly given that pure red noise processes can frequently mimic few-cycle sinusoid-like quasi-periods, and that we only measure four “cycles” here. We follow the recommendation of [Vaughan et al. \(2016\)](#) that roughly five cycles are typically needed to distinguish between red noise and a true period. Finally, fully considering the “look elsewhere” effect means one should also take into account those X-ray power-spectra of Mkn 421 previously published and where a narrow power component was not claimed (e.g., [Chatterjee et al. 2018](#)). In conclusion, the observed quasi-periodic behaviour does not indicate significant deviation from a pure red-noise process.

This paper has been typeset from a \LaTeX file prepared by the author.